The Planetary Science Journal, 6:199 (28pp), 2025 August https://doi.org/10.3847/PSJ/adec6b


# Ejecta Mass Estimates from the DART Impact Plume Inferred from LICIACube Images

Ramin Lolachi[1,2,3], David A. Glenar[1,2,3], Timothy J. Stubbs[2], Ludmilla Kolokolova[4], Olga Muñoz[5], Tony L. Farnham[4], Masatoshi Hirabayashi[6], Pedro H. Hasselmann[7], Vincenzo Della Corte[8], J. D. Prasanna Deshapriya[7], Elisabetta Dotto[7], Elena Mazzotta Epifani[7], Alessandro Rossi[9], and Angelo Zinzi[10,11]
[1] Center for Space Sciences and Technology, University of Maryland, Baltimore County, Baltimore, MD 21250, USA; rlolachi@umbc.edu, ramin.lolachi@nasa.gov
[2] NASA Goddard Space Flight Center, Greenbelt, MD 20771, USA
[3] Center for Research and Exploration in Space Science and Technology, NASA/GSFC, Greenbelt, MD 20771, USA
[4] University of Maryland, College Park, MD 20742, USA
[5] Instituto de Astrofísica de Andalucía, CSIC, Glorieta de la Astronomía sn, Granada, 18008, Spain
[6] Daniel Guggenheim School of Aerospace Engineering, Georgia Institute of Technology, 620 Cherry Street, Atlanta, GA 30332, USA
[7] INAF–Osservatorio Astronomico di Roma Via Frascati 33, I-00078 Monte Porzio Catone (Rome), Italy
[8] Osservatorio Astronomico di Capodimonte, INAF, Naples, Italy
[9] IFAC-CNR, Sesto Fiorentino, I-50019, Italy
[10] Space Science Data Center, ASI, Rome, Italy
[11] Agenzia Spaziale Italiana, Rome, Italy
*Received 2025 February 18; revised 2025 June 13; accepted 2025 July 3; published 2025 August 21*

## Abstract

We report ejecta mass estimates produced by the Double Asteroid Redirection Test impact with Dimorphos, the secondary of the Didymos asteroid binary system. This first demonstration of an asteroid deflection technique was witnessed by the Light Italian Cubesat for Imaging of Asteroids (LICIACube). The LICIACube Unit Key Explorer (LUKE) RGB camera images are used to estimate the ejecta mass, critical to understanding the impact conditions and physical properties of the asteroid. This requires realistic scattering properties for the ejecta particles, which were obtained from model and laboratory scattering analog particles (sizes $<1$ $\mu$m to $\sim$1 cm). The particle size distribution (PSD) of ejecta is constrained from a series of 18 images acquired at widely separated phase angles (50.°6 to 110.°2) using the size dependence of the analog scattering phase functions. Total plume radiance in the LUKE RGB channels is determined by spatially integrating over the field of view in each image. Plume radiances are then used to retrieve ejecta mass assuming an optically thin plume, giving lower limit estimates of 0.85 to $1.19 \times 10^7$ kg. Results indicate that the PSD of ejecta in the nascent plume follows a single power-law coefficient ($k \approx -2.5$), rather than the broken power law inferred from later observations. Using a single, high signal-to-noise image, the observed areal mass-brightness relation is extrapolated inward, yielding an increase of $\approx$77% for ejecta mass in the optically thick inner region. Our ejecta mass estimates are consistent with Dimorphos having weak cohesive strength ($<$5000 Pa but more likely $\sim$50 Pa).

*Unified Astronomy Thesaurus concepts:* Asteroids (72); Asteroid satellites (2207); Impact phenomena (779); Near-Earth objects (1092); Radiative transfer (1335)

## 1. Introduction

The Double Asteroid Redirection Test (DART) mission was the world's first planetary defense mission dedicated to demonstrating a potential mitigation approach (N. L. Chabot et al. 2024). After reaching the binary (65803) Didymos-Dimorphos asteroid system (believed to be S-type; J. de León et al. 2006; D. Polishook et al. 2023), it hit the $\approx$160 m diameter secondary, Dimorphos, on 2022 September 26 at 23:14 UTC (R. T. Daly et al. 2023). Impacting at a speed of 6.1 km s$^{-1}$, it successfully demonstrated the kinetic impact deflection technique by reducing Dimorphos' orbital period about Didymos by 33 minutes $\pm$1 ($3\sigma$) (C. A. Thomas et al. 2023a). In the following months, this was refined by P. Scheirich et al. (2024) to 33.24 minutes $\pm$0.072 ($3\sigma$) and by S. P. Naidu et al. (2024) to 32.75 minutes $\pm$0.025 ($1\sigma$).

Close proximity observations of the impact and ejecta in the first few minutes were made by the Light Italian Cubesat for Imaging of Asteroids (LICIACube) developed by the Italian Space Agency (ASI; E. Dotto et al. 2021). Two imagers aboard LICIACube captured the impact: the LICIACube Explorer Imaging for Asteroid (LEIA) narrow-field monochrome camera, and the LICIACube Unit Key Explorer (LUKE) wide-field RGB camera. The observations showed a complex inhomogeneous ejecta plume with filamentary structures (Figure 1) (E. Dotto et al. 2024).

Using these LUKE flyby images of the ejecta, T. L. Farnham et al. (2025) tracked the 3D trajectories of 104 boulders with radii up to 3.6 m and ejection speeds up to 52 m s$^{-1}$. The 104 boulders were estimated to have mass of $9.7 \times 10^5$ kg, using an assumed density of 2400 kg m$^{-3}$, the same as the Dimorphos bulk density. This is a lower limit as the boulder density is likely higher than the bulk density assumed (boulders are likely to be monolithic and contain less void space), not all detected boulders were used in the analysis, and there may be other boulders undetected. It was calculated that the momentum associated with the boulders is comparable to that of the spacecraft and the corresponding recoil could have changed the inclination of Dimorphos' orbital plane by up to 1° and cause Dimorphos to tumble.

Other early-stage observations of the impact and period immediately after came from a number of ground-based

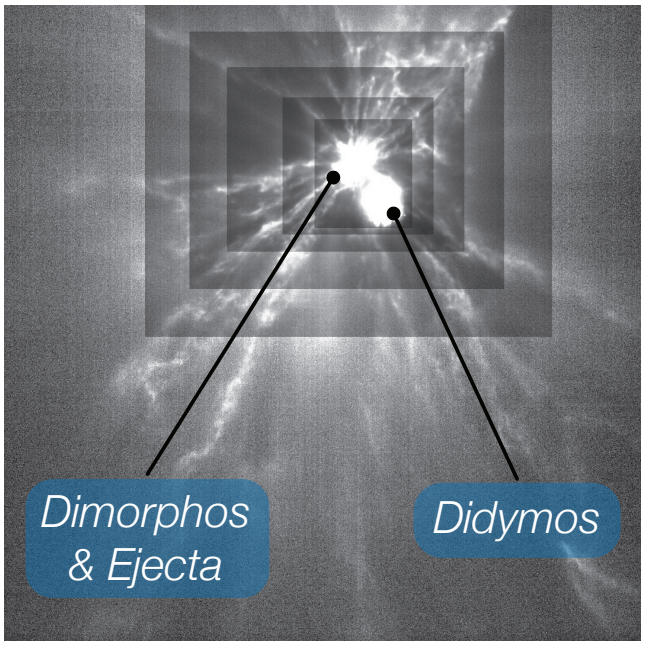


**Figure 1.** LICIACube image (adapted from Figure 5 from N. L. Chabot et al. 2024) acquired at $t = 143$ s after impact of the DART spacecraft, showing a complex system of ejecta rays with filamentary structures. Each rectangle represents a different level of contrast in order to better see the fine structure in the ejecta. The innermost rectangle is roughly 1.3 km wide. (LICIACube LUKE image triplet acquired at 23:16:47 UTC; Credit: ASI/NASA/APL.)

telescopes (A. Fitzsimmons et al. 2023; A. Graykowski et al. 2023; L. Shestakova et al. 2023; N. L. Chabot et al. 2024) and the Lucy mission (H. A. Weaver et al. 2024). They showed the release of an initial plume of fast material immediately after impact with speeds of 1 to 3.6 km $s^{-1}$, before the release and formation of the slower (tens to hundreds of meters per second) main ejecta cone as determined from LICIACube observations by E. Dotto et al. (2024). Upper-limit mass estimates for the initial fast plume are hundreds to thousands of kilograms (A. Fitzsimmons et al. 2023; A. Graykowski et al. 2023; H. A. Weaver et al. 2024), a small fraction of the total ejecta mass (see Table 2).

Evolution of the ejecta cone in the hours after impact was observed by the Hubble Space Telescope (HST; J.-Y. Li et al. 2023), James Webb Space telescope (JWST; C. A. Thomas et al. 2023b), and ground-based telescopes (a detailed list is given in N. L. Chabot et al. 2024). Analysis of ejecta geometry from HST and LICIACube show it to be an ellipsoidal cone with a wide opening angle of $\approx 140^\circ$ and a narrow opening angle of $\approx 100^\circ$ (J. D. P. Deshapriya et al. 2023; M. Hirabayashi et al. 2025).

Over the following days and weeks after impact, long-term observation campaigns of the Didymos system and ejecta by the HST and ground-based telescopes showed Dimorphos had become an active asteroid (T. Kareta et al. 2023; J.-Y. Li et al. 2023; Z.-Y. Lin et al. 2023; F. Moreno et al. 2023; B. P. Murphy et al. 2023; C. Opitom et al. 2023; A. Rożek et al. 2023; Z. Gray et al. 2024; T. Lister et al. 2024). Solar radiation pressure (SRP) acting on the smallest ejected particles led to the formation of a dust tail. This is because SRP has a greater effect on smaller particles, as it is inversely proportional to particle radius (J.-Y. Li et al. 2023). In addition to dust particles, much larger ejecta was observed escaping the Didymos system. Using HST observations from 2022 December, D. Jewitt et al. (2023) tracked a population of 37 boulders ($\sim$1 m) launched by the impact with an estimated mass of $\approx 5 \times 10^6$ kg, using an assumed density of 2200 kg $m^{-3}$. Their mean sky-plane velocity dispersion of $0.30 \pm 0.03$ m $s^{-1}$ was only slightly greater than the Didymos system escape velocity (0.24 m $s^{-1}$). The boulder group was estimated to carry only a tiny fraction of the DART impact's kinetic energy ($\approx 3 \times 10^{-5}$).

Calculating the momentum enhancement factor $\beta$ of the DART impact was the DART-4A Level 1 mission requirement (A. S. Rivkin et al. 2021; N. L. Chabot et al. 2024). By definition, $\beta = 1$ for an inelastic collision with no ejecta (K. R. Housen & K. A. Holsapple 2011). Calculations using Monte Carlo models by A. F. Cheng et al. (2023) estimated $\beta = 3.6^{+0.19}_{-0.25}(1\sigma)$, assuming a Dimorphos bulk density of 2400 kg $m^{-3}$, where the largest uncertainty source is the mass of Dimorphos. ESA's upcoming HERA mission is expected to measure Dimorphos' mass (P. Michel et al. 2022). All estimates have determined that $\beta > 2$, which means that more momentum is imparted to Dimorphos from the impulse of the ejecta than from the incident spacecraft (A. S. Rivkin et al. 2021; A. F. Cheng et al. 2023). This ejecta impulse is analogous to the momentum change provided by the thrust of a rocket engine.

Characterizing ejecta properties, particularly ejecta mass plays an important role in the DART-4B Level 1 objective to investigate the Didymos-Dimorphos system and changes resulting from DART's impact (A. S. Rivkin et al. 2021; N. L. Chabot et al. 2024). Ejecta mass is an integral part in the characterization of ejecta momentum, and also informs calculations of $\beta$ (A. S. Rivkin et al. 2021; A. F. Cheng et al. 2022). Ejecta mass places constraints on the material properties of the asteroid, particularly strength and porosity (A. S. Rivkin et al. 2021; A. F. Cheng et al. 2024; S. D. Raducan et al. 2024). These constraints can then be applied to impact models, reducing the parameter space that needs to be searched and ultimately refining calculations of $\beta$, also part of DART-4B (A. S. Rivkin et al. 2021; A. F. Cheng et al. 2024; S. D. Raducan et al. 2024). Every additional constraint is crucial, as $\beta$ is nonunique with many combinations of parameters leading to the same value (A. F. Cheng et al. 2023, 2024).

To date, ejecta mass estimates have been calculated using numerical simulations (Y. Kim & D. Jewitt 2023; F. Moreno et al. 2023; A. F. Cheng et al. 2024; F. Ferrari et al. 2025), ground-based observations (A. Graykowski et al. 2023; N. X. Roth et al. 2023), and HST images (D. Jewitt et al. 2023; J.-Y. Li et al. 2023). A list of these mass estimates is given in Table 2 (a more comprehensive list can be found in D. C. Richardson et al. 2024). Image data from the closest observer of the DART impact, LICIACube, has been used to constrain ejecta models (A. F. Cheng et al. 2024; S. D. Raducan et al. 2024; A. M. Stickle et al. 2025), but until this study, no direct estimates of eject mass have been made using this unique data set.

Observations of sunlight scattered by ejecta from the DART impact provide a means to characterize ejecta properties, including mass (A. Graykowski et al. 2023; J.-Y. Li et al. 2023; Z. Gray et al. 2024). This requires some knowledge of scattering properties and the ejecta particle size distribution (R. Lolachi et al. 2023b).

In this study we obtain total plume brightness at widely separated phase angles (Observer-Dimorphos-Sun angle) to constrain both particle size distribution and plume mass in the

**Table 1**
LICIACube Observation Data Used for This Study

| Image Index [#] | L1+ Filename | UTC | $t$ (s) | $\alpha$ (°) | $d$ (km) | Pixel IFOV (m px$^{-1}$) | $r_b$ (px) | $r_b$ (m) | Location | Quality |
|---|---|---|---|---|---|---|---|---|---|---|
| 0* | 1664234204_00505_01 | 23:16:44.050 | 139.87 | 52.4 | 177.9 | 13.88 | 274 | 3803 | pre-CA | wide-field |
| 1 | 1664234210_00002_01 | 23:16:50.000 | 145.82 | 51.4 | 144.3 | 11.26 | 209 | 2353 | pre-CA | partially clipped |
| 2 | 1664234213_00004_01 | 23:16:53.000 | 148.82 | 50.9 | 127.9 | 9.98 | 226 | 2255 | pre-CA | partially clipped |
| 3 | 1664234216_00003_01 | 23:16:56.000 | 151.82 | 50.6 | 112.2 | 8.75 | 159 | 1391 | pre-CA | partially clipped |
| 4 | 1664234219_00002_01 | 23:16:59.000 | 154.82 | 50.6 | 97.5 | 7.61 | 74 | 563 | pre-CA | heavily clipped |
| 5 | 1664234220_00005_01 | 23:17:00.000 | 155.82 | 50.8 | 92.9 | 7.25 | 47 | 341 | pre-CA | heavily clipped |
| 6 | 1664234222_00002_01 | 23:17:02.000 | 157.82 | 51.5 | 84.3 | 6.58 | 42 | 276 | pre-CA | heavily clipped |
| 7 | 1664234223_00005_01 | 23:17:03.000 | 158.82 | 52.1 | 80.3 | 6.26 | 96 | 601 | pre-CA | heavily clipped |
| 8 | 1664234224_00003_01 | 23:17:04.000 | 159.82 | 52.9 | 76.7 | 5.98 | 47 | 281 | pre-CA | heavily clipped |
| 9 | 1664234241_00007_01 | 23:17:21.000 | 176.82 | 94.4 | 87.4 | 6.82 | 114 | 777 | post-CA | heavily clipped |
| 10 | 1664234242_00003_01 | 23:17:22.000 | 177.82 | 96.2 | 91.8 | 7.16 | 187 | 1339 | post-CA | partially clipped |
| 11 | 1664234243_00002_01 | 23:17:23.000 | 178.82 | 97.7 | 96.3 | 7.51 | 222 | 1667 | post-CA | partially clipped |
| 12 | 1664234244_00007_01 | 23:17:24.000 | 179.82 | 99.2 | 101.1 | 7.89 | 236 | 1862 | post-CA | partially clipped |
| 13 | 1664234247_00003_01 | 23:17:27.000 | 182.82 | 102.7 | 116.1 | 9.06 | 324 | 2935 | post-CA | partially clipped |
| 14* | 1664234250_00005_01 | 23:17:30.000 | 185.82 | 105.3 | 131.9 | 10.29 | 340 | 3499 | post-CA | wide-field |
| 15 | 1664234253_00005_01 | 23:17:33.000 | 188.82 | 107.3 | 148.4 | 11.58 | 302 | 3497 | post-CA | wide-field |
| 16 | 1664234256_00005_01 | 23:17:36.000 | 191.82 | 108.9 | 165.3 | 12.9 | 271 | 3496 | post-CA | wide-field |
| 17 | 1664234259_00003_01 | 23:17:39.000 | 194.82 | 110.2 | 182.5 | 14.24 | 245 | 3489 | post-CA | wide-field |

**Note.** Columns headers: L1+ Filename is the Level 1+ LICIACube observation image filename, UTC is time of observation in Coordinated Universal Time, $t$ is time elapsed in seconds after DART impact, $\alpha$ is the observation phase angle (Observer-Dimorphos-Sun angle), $d$ (target distance) is the distance between LICIACube and Dimorphos, Pixel IFOV is the pixel instantaneous field of view (FOV), and $r_b$ defines the radial extent of the circular plume brightness integration region. Observations before closest approach (CA) are designated "pre-CA" and those after "post-CA" in the Location column. Observation quality is given in the Quality column, where "wide-field" indicates an image in which the plume is far enough away from the edge of the FOV for the annular integration of plume brightness to capture all plume light above the LUKE detection limit. Images with the plume closer to the FOV edge, but usable, are designated "partially clipped," and those with extreme clipping (not used in data fitting procedures) are designated "heavily clipped" ($r_b < 1000$ m). Asterisk (*) entries indicate reference images.

optically thin approximation. This is achieved by using the size and phase-angle dependence of the particle scattering phase function. However, the innermost region of the plume is optically thick. In the case of one optimal image, it was possible to estimate empirically the additional mass in the optically thick region (optical depth $\gtrapprox 0.2$; see Sections 3.2 and 5) by inward extrapolation of the observed areal mass–brightness relation. Together, these findings allow us to estimate both lower limits and a single upper-limit determination of the near-field ejecta mass, with uncertainties.

A direct product of the retrieval is the ejecta particle size distribution. Previous work using HST observations of the ejecta tail suggested a broken power-law size distribution (J.-Y. Li et al. 2023; F. Moreno et al. 2023). However, it seems that despite starting with this assumption for our study, the LICIACube observations are best fit with a single power-law distribution, implying some sort of size-sorting process (e.g., driven by SRP) of ejecta particles occurred between the LICIACube observations and the later HST observations. This result is not surprising, since the LICIACube observations were made minutes after impact, while SRP effects were observed hours later in the far-field HST observations. We discuss this finding in further detail in Section 4.

In Section 2 we describe the process of obtaining plume radiance measurements from LICIACube data. In Section 3 we describe our family of scattering models for impact plume ejecta fragments ranging in size from submicron to decimeter scales. In Section 4 we apply these scattering phase functions to our forward models and use them to retrieve mass from the optically thin portion of the plume. In Section 5 we assess possible mass enhancements from the optically thick portion of the plume. In Section 6 we discuss our findings and compare our results with the mass estimates of others discussed above. Finally, we summarize our findings and their implications in Section 7.

## 2. Plume Radiance Measurements

During the LICIACube flyby, the LUKE RGB camera acquired a sequence of images at approximately 3 s cadence. The LICIACube data used in this study are an early-access (Level 1+) version released to the team around 2023 March 30. This version of the data set had been color-separated with bad pixels identified, converted from DN to floating point and corrected for nonlinearities. A copy of this data is available on Zenodo: doi:10.5281/zenodo.14509702 (R. Lolachi et al. 2024). Linearity in the LUKE response for each RGB channel was checked using an integrating sphere prior to launch during ground calibration (A. Zinzi & V. Della Corte 2023) and repeated in-flight by the LICIACube team using measurements of $\xi^2$ Ceti at multiple integration times. Additional verification of linearity was performed during this study as part of the absolute radiometric calibration using observations of the Pleiades and $\xi^2$ Ceti, as detailed in Appendix A.

Images were used where the plume was largely within the field of view (FOV), and target distance was <200 km. Observing circumstances for the selected set of images are listed in Table 1. Figure 2 summarizes these circumstances graphically and illustrates the data gap that is more-or-less centered on the time of closest approach (CA). In Figure 2(A) the $x$-, $y$-, and $z$-axes form an orthogonal set, with the plume cone centered on the $y$-axis, where the DART impact trajectory corresponds to the negative-$y$-direction. The $x$–$y$ plane is defined by the LICIACube trajectory (also along negative $y$) and its line of sight (LOS). In Figure 2(B), the data gap around CA is due to the fact that the plume and Dimorphos moved out of the LUKE FOV as

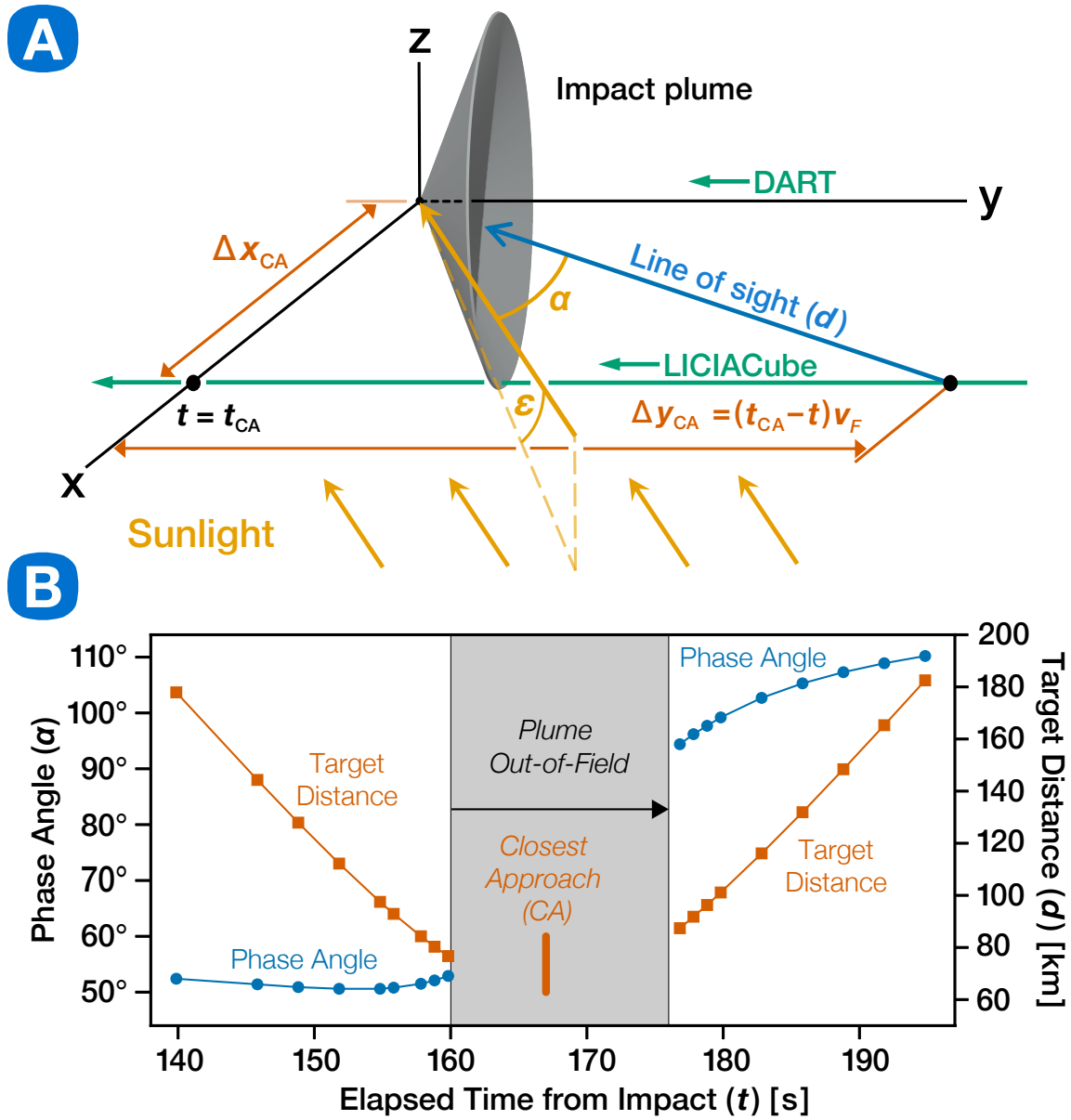


**Figure 2.** (A) LICIACube encounter with evolving optical scattering geometry: LICIACube Flyby Geometry based on A. F. Cheng et al. (2020); origin at impact and ejecta plume centered on the $y$-axis. The "Line of-sight" is the reverse of the position vector (as function of time) of LICIACube and $v_F$ is the relative velocity of LICIACube; $\Delta x_{CA}$ is the distance from the origin at closest approach ($t = t_{CA} = 167$ s); $\alpha$ is the phase angle, i.e., $180° - \theta$, where $\theta$ is the scattering angle, and $\varepsilon$ is the Sun elevation angle. (B) Observing circumstances for LICIACube observations of the DART impact plume, during approach and flyby of Dimorphos.

LICIACube attempted to track the asteroid. The image set spans a phase-angle range of 50.°6 to 110.°2 and enables some particle size discrimination as a result of the size dependence of the phase curve shape (Section 3). Image data is cropped to 1024 × 1024 RGB subframes, with each subframe centered on Dimorphos using SPICE kernels and trajectory solutions as detailed in T. L. Farnham et al. (2025). Images marked "wide-field" extend radially to at least 3.5 km before encountering the frame edge (i.e., in the image plane, which contains Dimorphos and is perpendicular to the look direction), and capture all plume light detectable above the LUKE noise level.

### 2.1. LUKE Responsivity and Conversion to Radiance

The LUKE RGB channels were calibrated to absolute response by comparing measurements of eight Pleiades stars acquired during the approach phase, to the Johnson-Cousins/JC UBVRI (M. S. Bessell 1990) magnitudes of those stars as listed in the SIMBAD object database (https://simbad.u-strasbg.fr/simbad/). For each star, we computed the average flux (W m$^{-2}$ nm$^{-1}$) at the effective wavelengths of the JC filter bands. Procedurally, this is done using the spectral flux from Vega (R. C. Bohlin et al. 2014), and then applying magnitude ratios. The resulting set of node fluxes is interpolated to create a piecewise linear approximation for the star's spectrum, and that spectrum is then integrated over the known LUKE filter shapes (G. Poggiali et al. 2022) to get the corresponding RGB band fluxes. This calibration procedure resulted in derived scale factors and uncertainties of $S_R = 0.056 \pm 0.010$, $S_G = 0.060 \pm 0.008$, and $S_B = 0.113 \pm 0.031$, that convert the measured L1+ pixel signals to scene radiance, W m$^{-2}$ sr$^{-1}$ nm$^{-1}$ in each band. A full description of the response calibration steps is described in Appendix A.

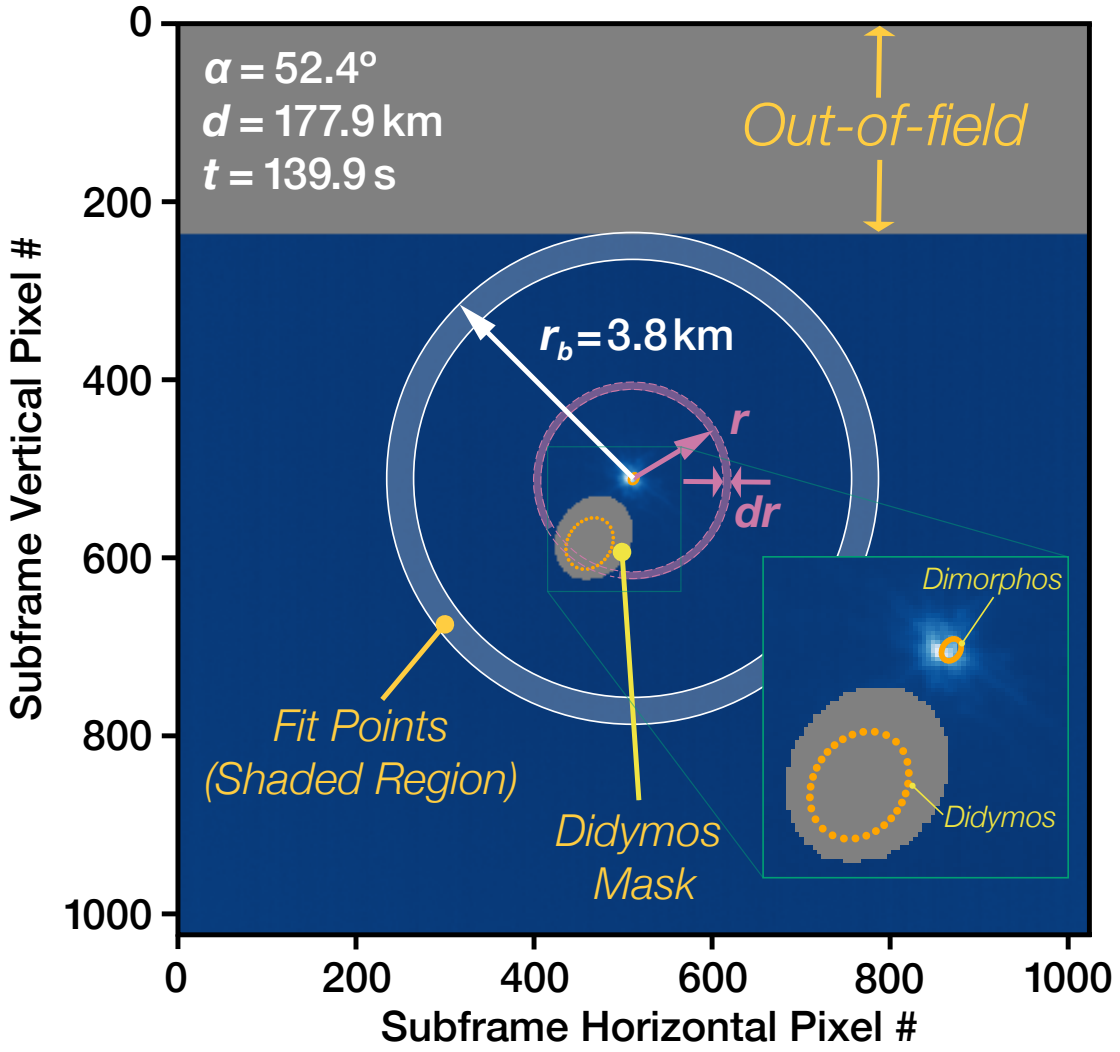


**Figure 3.** Bias correction and plume spatial integration geometry for wide-field images, illustrated by a sample 1024 × 1024 LUKE frame centered on Dimorphos. Didymos and Dimorphos outlines are in orange, and Didymos light is removed using an oversized mask elongated in the Sun direction. The annular blue-gray area defines the pixel values used to apply a planar fit to the bias surface. The outer radius defines the spatial integration region for plume light, computed by radially summing the azimuthally averaged signal, excluding Didymos (pink band) in addition to remaining stray light observed beyond the mask edge. (Inset) Zoomed-in detail of the image center showing Didymos, Dimorphos, and ejecta.

### *2.2. Estimating Total Plume Radiance*

Ideally, the calibrated images can be spatially integrated and compared with models of total plume radiant intensity to constrain both plume mass and grain size that dominate the observable light. However, there are significant obstacles to these goals that we attempt to circumvent, namely:

1. Changes in the plume mass and shape over the flyby observation period used in this study. The images from LICIACube suggest that the ejecta release is ongoing at CA (J. D. P. Deshapriya et al. 2023; E. Dotto et al. 2024), supported by a crater formation timescale >600 s (M. Hirabayashi et al. 2022).
2. A spatially variable bias (that likely includes some background contributions) exists in each image for the purpose of eliminating bad pixels and avoiding negative excursions in pixel values.
3. An oversized Didymos mask must be added in each image to reject its light, but this creates an obscuration, in addition to low-level stray light observed beyond the mask edge.
4. In many of the images, an unknown fraction of the plume light lies beyond the frame boundaries, as the plume drifts in and out of the LUKE FOV during flyby. This is demonstrated by Figure 1 (Figure 5 in N. L. Chabot et al. (2024)), which shows the detectable extent of the nascent plume extends to at least several kilometers.

Issue (1) relates to our assumption of an essentially static (steady state) plume over the course of observations used in this study. This is addressed by noting that the duration of observations used for this study is ≈55 s, which is a small fraction (<10%), of the crater formation timescale of >600 s (M. Hirabayashi et al. 2022). This suggests little significant change in mass or shape should be expected over the study observation period. This is also supported by examining an animation of the LICIACube images close to CA ($t$ = 140 to 190 s, the same as this study), provided in the supplemental material of T. L. Farnham et al. (2025), which shows no appreciable change in plume morphology during flyby.

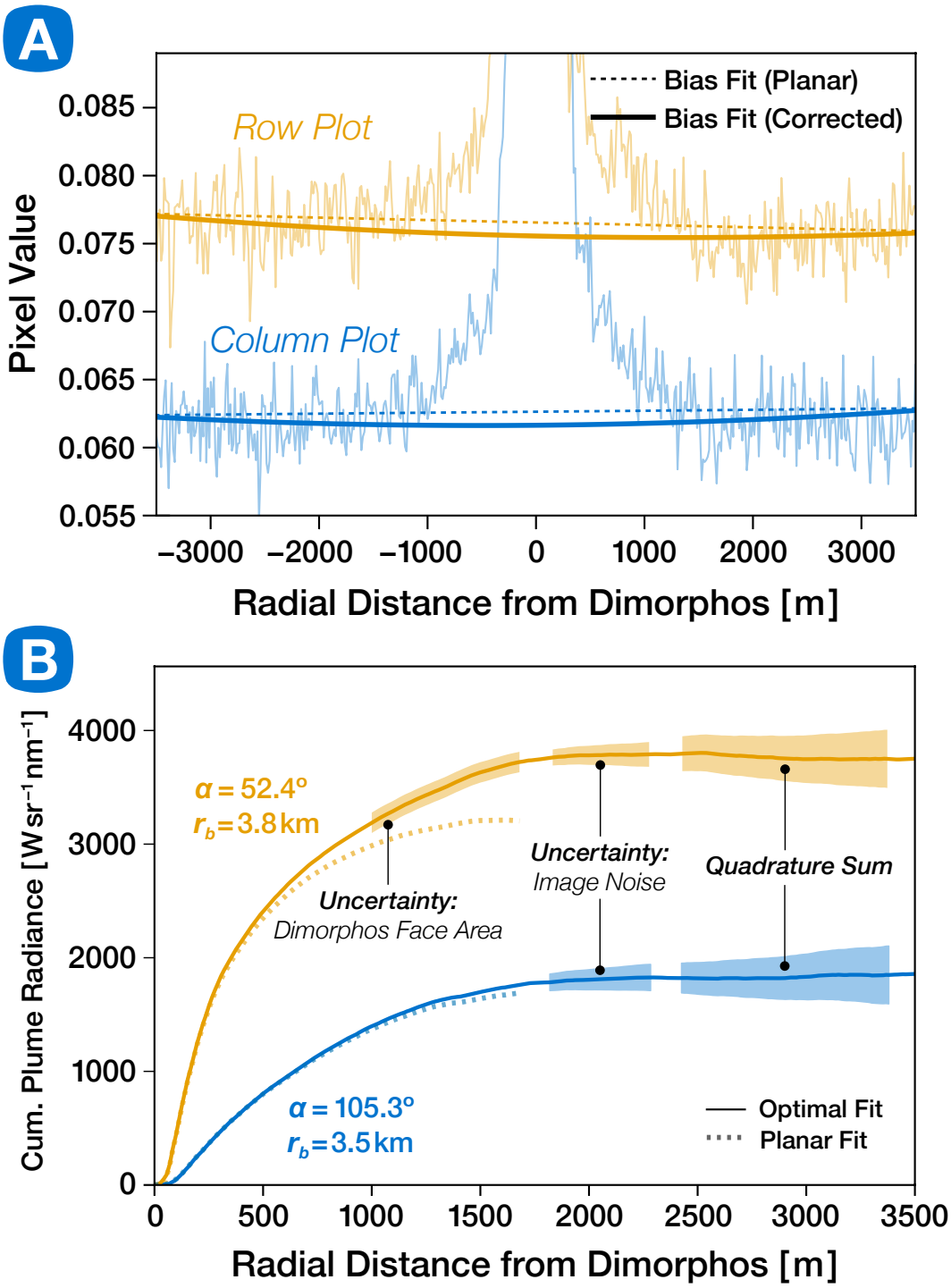


**Figure 4.** Radiance measurements in the green channel for wide-field images. (A) Sample row (orange) and column (blue) plots, through Image #0 center, compared with cuts through the planar bias surface $b_p(r, \theta)$, shown as dotted lines. Solid lines show the concavity-corrected models $b(r, \theta)$, needed to flatten the cumulative radiance curve. (B) Cumulative radiance profiles $I(r)$ for pre- and post-close-approach integrations (Images #0 [orange] and #14 [blue] in Table 1). Sources of uncertainty (shaded bands) are discussed in Section 2.4

Although local changes in plume LOS optical depth will occur due to ejecta motion, the spatially integrated mass over the FOV should remain nearly constant.

Figure 3 shows the geometry used to model the bias surface and sum the net scattered light in the wide-field images. Only five of the images, which we refer to as wide-field (Table 1), are far enough away from FOV boundaries to capture all plume light above the LUKE detection limit; i.e., where plume brightness falls below the image noise. The plume light measurement is confined to a circular region with radius $r_b$ at the target distance, centered on Dimorphos and bounded by the edge of the FOV. Image bias is removed by defining an annular region between 0.9 and 1.0 $r_b$ (blue-gray shaded region). Points in this annulus are fit to a three-coefficient, planar approximation $b_p(r, \theta)$ for the interior region, with $\theta$ being the azimuthal coordinate. In wide-field cases, the

annulus is negligibly influenced by plume radiance but provides sufficient pixel statistics for accurately computing the bias value. Figure 4(A) shows an example of a planar fit result (dotted line) superimposed on row and column plots through the center of Image #0. Plume light is then estimated by summing narrow rings to create cumulative radiance curves extending from the center to $r_b$.

In this and other wide-field cases, some additional concavity is detectable in regions of high scene brightness. The reason for this is not clear, but we improve the baseline correction using a centered Cauchy distribution with small amplitude $f$ (a few $\times$ 0.01), adjusted as described below,

$$b(r, \theta) = b_p(r, \theta)\left\{1 - f\left[1 - \left(\frac{r}{r_b}\right)^2\right]\right\}. \quad (1)$$

The azimuthally averaged intensity in each contributing ring is then,

$$\overline{I_{\rm ring}}(r) = \frac{1}{\theta_E}\int_{\theta_E}[I_{\rm px}(r, \theta) - b(r, \theta)]\, d\theta, \quad (2)$$

with $\theta_E$ being the set of azimuthal angles that exclude the Didymos mask. Narrow ring contributions are then added to construct a cumulative radiance profile,

$$I(r) = \int_{0,r_{\rm D}}^{r} 2\pi u\, \overline{I_{\rm ring}}(u)\, du. \quad (3)$$

Prior to CA, the plume lies in the foreground, and the unknown optical depth makes it uncertain as to whether or not to include the Dimorphos radius as the lower integration limit of Equation (3), so this central contribution becomes one of the uncertainties named below. Beyond CA, the observing perspective shows Dimorphos separated from the plume, and the lower integration limit is $r_{\rm D}$. Designating $i$ as image index, the asymptotic value of $I(r)$ gives the measured plume radiant intensity $I_i$, or $I(a_i)$ as referred to in Sections 3 and 4. The amplitude $f$ is then fine adjusted to make the cumulative radiance profiles asymptotically flat, as shown in the examples of Figure 4(B).

### 2.3. Adjustments for Spatially Truncated Images

Images designated "partially clipped" in Table 1 are also usable if we assume that plume shape does not change appreciably over the ≈20 s pre-CA or ≈18 s post-CA image duration (see Section 2.2). For these images, we approximate $I(r)$ by recognizing that, for $r < r_b$, a clipped image profile $I_{\rm cl}(r)$ is the product of a wide-field reference $I_{\rm ref}(r)$ and an unknown, phase-angle-dependent albedo ratio $A(\alpha)/A_{\rm ref}$. The other term is a uniform, downward bias shift $\Delta B$ that accounts for uncaptured radiance. The equation relating these profiles is

$$I_{\rm cl}(r) = \left(\frac{A(\alpha)}{A_{\rm ref}}\right)I_{\rm ref}(r) - \Delta B\pi r^2 \qquad (r \leqslant r_b). \quad (4)$$

As reference profiles, we choose wide-field Images #0 and #14 for the pre- and post-CA series, respectively. A $\chi^2$ minimization is carried out to solve for values of $A/A_{\rm ref}$ and $\Delta B$ that achieve the best shape correlation between $I_{\rm cl}$ and $I_{\rm ref}$ up to the boundary radius $r_b$. Specifically, for each set of $r_j \leqslant r_b$, we minimize

$$\chi^2\left(\frac{A(\alpha)}{A_{\rm ref}}, \Delta B\right) = \sum_{r_j \leqslant r_b}\frac{\left[I_{\rm cl}(r_j) + \Delta B\pi r_j - \left(\frac{A(\alpha)}{A_{\rm ref}}\right)I_{\rm ref}(r_j)\right]^2}{I_{\rm cl}(r_j)} \quad (5)$$

The effect is to transform the uncorrected truncated shape $I_{\rm cl}$ to a scaled version of the reference shape, i.e., $I(r) = (A(\alpha)/A_{\rm ref}) \cdot I_{\rm ref}(r)$. Figure 5 illustrates the radiance correction method, using post-CA index #10 as subject image.

### 2.4. Measurement Uncertainties

Obtaining the uncertainties in the plume radiance profiles requires a physical model for the spatial intensity distribution, which is not known a priori. Instead, we estimate the uncertainties to be the quadrature sum of three sources: As commented above, one source is the unknown plume contribution within the Dimorphos outline, which applies only to pre-CA images. The other two sources are obtained from fit statistics: A significant contribution comes from the annular fit near the $r_b$ boundary, and depends largely on signal-to-noise ratio (SNR). This is approximated using the diagonal elements of the $3 \times 3$ fit covariance matrix. Noting that $\partial B/\partial c_0$, $\partial B/\partial c_x$, and $\partial B/\partial c_y$ equals 1, $x$, and $y$, respectively (ignoring the perturbation factor $f$), this error source $\epsilon$ is

$$\epsilon(x, y) = \sqrt{{\rm cov}_0 + x^2{\rm cov}_x + y^2{\rm cov}_y}. \quad (6)$$

This source can be thought of as a perturbation in the underlying fit surface, and the corresponding uncertainty $\Delta I(r)$ is obtained from Equation (3), by substituting $b(r, \theta) \pm \epsilon$ in Equation (2). A third component applies to the partially clipped images and arises from the $A/A_{\rm ref}$, $\Delta B$ retrievals. It is determined using the overall variance between $I_{\rm ref}$ and the $I(r)$ result,

$$\Delta I_{\rm clip} = \sqrt{\frac{1}{N_j}\sum_j\left[\left(\frac{A}{A_{\rm ref}}\right)I_{\rm ref}(r_j) - I(r_j)\right]^2} \qquad r \leqslant r_b, \quad (7)$$

with $N_j$ being the number of $r$ points. There is yet a fourth systematic error in the derived radiances arising from the stellar calibration of Section 2.1. This uncertainty is treated in the context of the plume mass estimates (Sections 4 and 5).

### 2.5. Radiance Results

The scatter plot in Figure 6 shows the results of the radiance estimates for the LUKE green channel, with error bars representing error sources 1 to 3. Symbol size is proportional to $r_b$, as illustrated in the image insets. As the field becomes spatially restricted, the truncation correction becomes less reliable, as evidenced by generally larger scatter in the radiance results. Results from images with $r_b < 1000$ m (marked "heavily clipped" in Table 1) are color-coded gray and are not used in the plume mass analysis.

## 3. Scattering Properties of Plume Particles

A quantitative understanding of scattered light intensity as a function of phase angle and particle size is necessary for relating plume radiance measurements to particle abundance, and therefore mass. While a range of nomenclature exists in the literature for describing optical scattering behavior, one

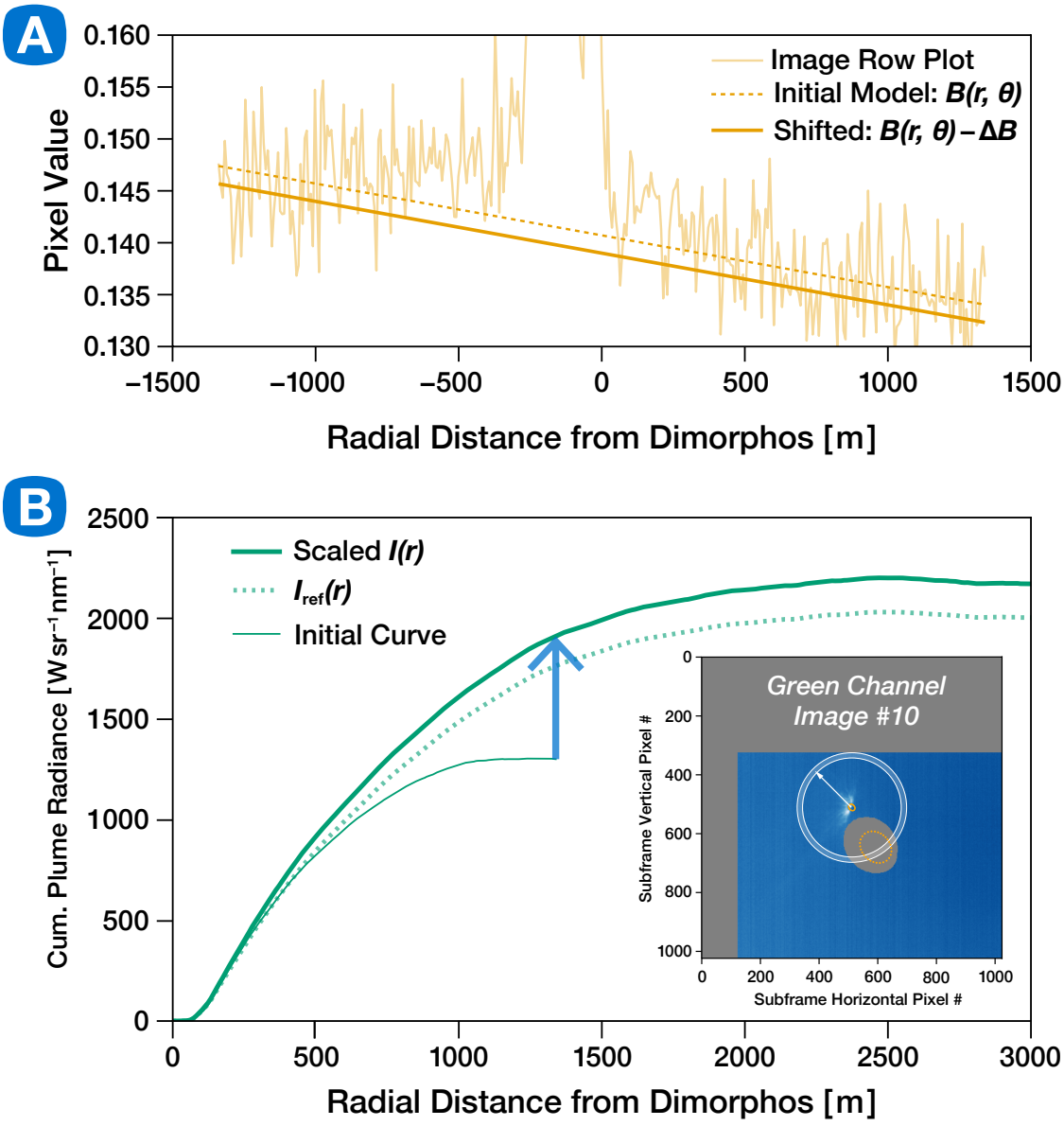


**Figure 5.** Illustration showing the shape-matching method for correcting radiance profiles of clipped images. A least-squares procedure is used to recover the albedo ratio $A/A_{\rm ref}$ and bias offset $\Delta B$ that accounts for plume radiance offset. These transform the truncated radiance curve to a scaled version of the reference shape (shown by blue arrow). (A) Central row plot from green channel, Image #10 ($\alpha = 96.^{\circ}2$) showing the retrieved downward shift $\Delta B$ of the bias model. (B) Thin green line shows the uncorrected radiance curve from post-CA Image #10 ($\alpha = 96.^{\circ}2$) that lies near the edge of the LUKE FOV (inset). The corrected $I(r)$ (thick green line) is the reference curve $I_{\rm ref}(r)$ (dotted green line) multiplied by $A/A_{\rm ref}$. In this example, $I_{\rm ref}(r)$ is taken from post-CA reference Image #14 at $\alpha = 105.^{\circ}3$.

approach uses the definition of zero-phase brightness expressed as physical (or geometric) albedo $A_{p0}$, defined as the ratio of a particle's zero-phase brightness, to that of a perfectly diffuse, equal-area Lambert disk (B. Hapke 2012). This definition can be extended to include the phase-angle dependence (M. S. Hanner et al. 1981; P. Pravec & A. W. Harris 2007), using the first element $F_{11}(\alpha)$ in the particle scattering matrix (K. Muinonen et al. 2009),

$$A_p(\alpha) = A_{p0}\frac{F_{11}(\alpha)}{F_{11}(\alpha = 0)}. \tag{8}$$

Typically, $F_{11}$ is azimuthally symmetric and normalized to $4\pi$ over a sphere, so that

$$\frac{1}{2}\int_0^{\pi} F_{11}(\alpha)\sin(\alpha)\, d\alpha = 1. \tag{9}$$

Designating a particle's specific intensity (W m$^{-2}$ sr$^{-1}$ nm$^{-1}$) by $I(\alpha)$, it's radiant intensity (W sr$^{-1}$ nm$^{-1}$) can then be written as

$$I(\alpha)\,\sigma_{\rm G} = \sigma_{\rm G}\,Q_{\rm sca}\,\frac{F_{11}(\alpha)}{4\pi}\bar{J}_{\odot}, \tag{10}$$

with $\sigma_{\rm G}$ being the particle geometric cross section ($=\pi a^2$, with $a$ being the spherical equivalent radius), $Q_{\rm sca}$ being the scattering coefficient, and $\bar{J}_{\odot}$ being the filter weighted solar flux in the LUKE R, G, and B channels, computed to be 1.65, 1.86, and 1.87 W m$^{-2}$ nm$^{-1}$, respectively. From the definition of $A_p$, it follows that the particle radiant intensity (W sr$^{-1}$ at phase angle $\alpha$ is

$$I(\alpha)\,\sigma_{\rm G} = A_p(\alpha)\,\sigma_{\rm G}\frac{\bar{J}_{\odot}}{\pi}, \tag{11}$$

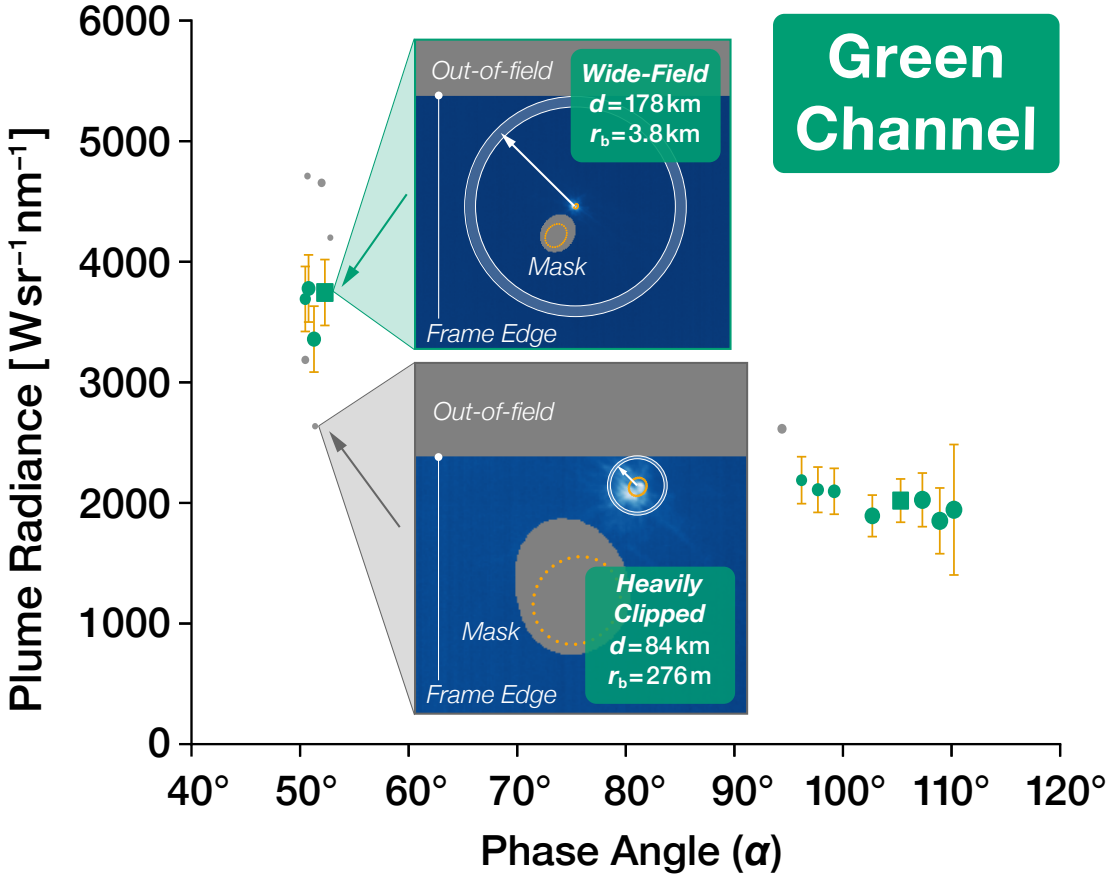


**Figure 6.** Scatter plot showing measured plume radiance in the green channel, with uncertainties. Large target distance (symbol size is proportional to distance) results in a wide plume capture area (up to ≈3.8 km) and confident estimates of cumulative radiance. At intermediate field sizes (marked "partially clipped" in Table 1), radiance is adjusted for clipping using a shape-matching procedure as described in the text and in Figure 5. This procedure becomes unreliable for heavily clipped cases (gray circles), where $r_b < 1$ km. These exhibit excessive scatter and are excluded from further analysis. Square points indicate reference images from Table 1. Inset images show examples of extreme cases.

and therefore,

$$A_p(\alpha) = Q_{\rm sca} \cdot F_{11}(\alpha)/4. \quad (12)$$

Alternatively, $Q_{\rm sca}$ can be replaced by the product of single-scattering albedo $\varpi$ and extinction coefficient $Q_{\rm ext}$, when those quantities can be estimated. Note also the equivalence of $\bar{I}_\odot/\pi$ to $\mathcal{F}$ in the definition of radiance factor (S. Chandrasekhar 1960; B. Hapke 2012), and thus, $A_p(\alpha)$ is recognized as the phase angle dependent particle radiance factor $I(\alpha)/\mathcal{F}$.

### 3.1. Derived Phase Curves

A set of geometric albedo curves for grain sizes spanning submicron to decimeter scales was compiled from a collection of models, laboratory measurements, and spacecraft observations. Measured scattering matrices and related references are available in the O. Muñoz et al. (2025) Granada–Amsterdam Scattering Database (https://scattering.iaa.es/). The set of curves, shown in Figure 8 and described in detail below is an extension of the family presented in R. Lolachi et al. (2023b). Representative sizes are listed in the figure. Particles in the laboratory samples are irregular in shape and, in this respect, are valid analogs for small plume fragments. Such shapes are typical of crushed powders (E. Zubko et al. 2013) and lunar grains (D. T. Richard et al. 2011), as well as material from airless bodies, including samples returned by spacecraft from asteroids such as Bennu (D. S. Lauretta et al. 2024) and Itokawa (an S-type like Didymos/Dimorphos; M. Yoshikawa et al. 2015). Particle albedo is also strongly influenced by refractive index, $m = \mathrm{Re}(m) + i\ \mathrm{Im}(m)$ ($\mathrm{Im}(m)$ is used here in place of $k$ to avoid confusion with power-law coefficient). Some constraints on $\mathrm{Im}(m)$ of DART impact plume particles were obtained by A. Penttilä et al. (2024) from ground-based polarization measurements. Results of that study were found to be consistent with a value of $\approx 1 \times 10^{-4}$. Where possible, analogs chosen for the present study are thus a mixture of carbonaceous asteroid material and samples of less absorbing Mg-rich olivine powders with $\mathrm{Im}(m) \approx 10^{-5}$ (E. Frattin et al. 2019). Particle scattering efficiencies are estimated using results of Discrete Dipole Approximation (DDA) computations (D. T. Richard et al. 2011; E. Zubko et al. 2017a) and, for larger particles, ray (geometric) optics methods with diffuse scattering (i.e., "RODS" models; K. Muinonen et al. 2009). The resulting suite of curves in Figure 8 reveals conspicuous trends in the phase-angle dependence of particle albedo that depend strongly on particle size; fine particles transition from flat to forward scattering at larger phase angles, whereas large fragments become monotonically dimmer with increasing phase over the range of LICIACube coverage. In the large size limit, phase curves are represented by that of the Didymos system itself. We consider this collection of curves to be gray (i.e., has no wavelength dependence) at visible wavelengths because of the limited scope of available samples, and the sporadic values of measured or sampled wavelengths.

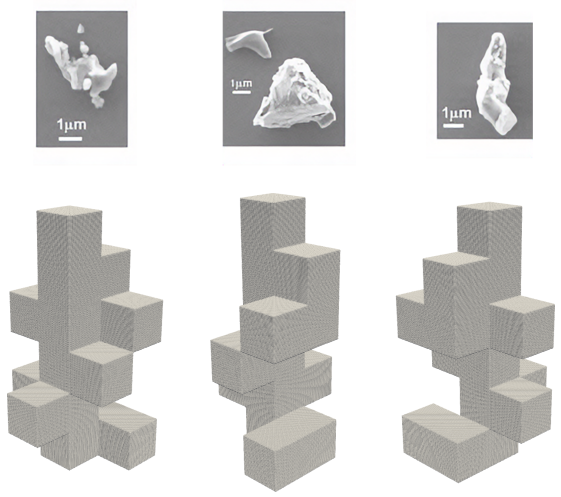


**Figure 7.** Top row: scanning electron micrographs of lunar dust grains from Apollo samples taken from J. S. Park et al. (2006) showing their jagged and irregular shape. Bottom row: corresponding DDA model showing the "Irregular" grain shape from three different rotated perspectives.

*Submicron*. The category for submicron particles ($a_{\rm eff} \leqslant 0.5\ \mu$m) uses phase curves originally used as models for scattering by ultra-fine lunar exospheric particles. They were created using results of DDA computations for several shapes as presented in R. Lolachi et al. (2023a) and R. Lolachi et al. (2025) building on work by D. T. Richard et al. (2011) using the DDSCAT software package (B. T. Draine & P. J. Flatau 1994). The shapes used for this study include prolate and oblate spheroids (ratios of 2:1 and 1:2 for the semimajor and semiminor axes), and the "irregular" grain shape based on scanning electron micrograph images of Apollo dust grains (see Figure 7). We used data from the three shapes at three wavelengths (442 nm, 562 nm, and 708 nm) to get a total of nine curves. We have taken the average (mean) of these curves to produce a single representative bold line, while the faint lines represent this average, plus or minus one standard deviation of the nine curves.

*Micron-Size*. This category is represented by averaging the scattering measurements of three ground meteorite powders typical of carbonaceous chondrites, with average $m = 1.65 + 0.001i$ (database samples Allende, FRO95002M, FRO99040M), with an equal number of brighter (Mg-rich) olivine samples with $\mathrm{Im}(m) \approx 1.62 \times 10^{-5}$ (O. Muñoz et al. 2000; E. Frattin et al. 2019; O. Muñoz et al. 2020). Effective radii, $a_{\rm eff}$, of the samples are the projected-surface-area weighted average radii obtained from particle sizer measurements, and lie between 2.6 and 5.9 $\mu$m. The average grain radius of all samples taken together is 4.40 $\mu$m. Measured phase functions ($\alpha = 3^\circ$ to $175^\circ$) exhibit broad and prominent forward scattering. In addition, a backscattering enhancement is exhibited by all powders. Normalized, $0^\circ$ to $180^\circ$ phase functions were constructed from the measurements following the methods outlined by those authors, as well as that of L. Liu et al. (2003): Extrapolation to $0^\circ$ phase is accomplished by applying the J. W. Hovenier & D. Guirado (2014) zero-slope condition to the smallest phase-angle points. At the largest phase angles, the measurement is scaled to merge with a forward scattering peak computed by weighting Lorenz-Mie diffraction shapes over the measured size distributions, recognizing that the diffraction peaks are not sensitive to particle shape. Normalizations of the complete phase functions are then fine adjusted (if needed) to $4\pi$ over $4\pi$ steradians. The other requirement is an estimate of particle scattering efficiency. This is traditionally challenging for particles in this size range, since size parameter $X = 2\pi a/\lambda$ (with $\lambda$ the wavelength) is generally too large for rigorous far-field computation such as DDA, but not large enough to be treated as geometric particles. Scattering properties of large, agglomerated debris particles as a function of refractive index and extending to size parameter 32 ($a \approx 3\ \mu$m) have been modeled by E. Zubko et al. (2017a, 2017b) using a modified DDA method. For $\mathrm{Im}(m) = 5 \times 10^{-4}$ (the smallest value in their series) and $X = 32$ (largest size parameter), those calculations lead to $Q_{\rm sca} \approx 2.2$. This value appears to remain nearly constant (i.e., asymptotic) with increasing grain size (A. A. Berezhnoy et al. 2019), so we consider it to be a reasonable estimate of $Q_{\rm sca}$ for the micron-size category. Figure 8 shows the $A_p$ curves predicted using this value in Equation (12). The bold line shows the surface-area weighted average curve for the collection of powders, and faint lines represent this average, plus or minus one standard deviation of the measured samples.

*Submillimeter*. We use scattering measurements ($\alpha = 6^\circ$ to $176^\circ$) of large Saharan (Libyan) sand grains as measured by O. Muñoz et al. (2007) using a 632.8 nm HeNe laser source. Projected area measurements based on Fraunhofer diffraction indicate effective radius $a_{\rm eff} \approx 125\ \mu$m, with the measured distribution spanning particle radii from $\approx$7 to 800 $\mu$m. As summarized by O. Muñoz et al. (2007), prior studies of Saharan sand particles from this region show $\mathrm{Re}(m)$ to be constrained between 1.5 and 1.7, while published measurements of $\mathrm{Im}(m)$ span more than an order of magnitude ($6 \times 10^{-4}$ to 0.025) due to variability in trace element concentration. As with the meteorite powders, these large particles exhibit broad forward scattering, although backscattering is observed to be nearly absent in this single example. It is significant to note that the entire size distribution can be treated as geometric particles or nearly so, as verified by the range of size parameter ($X = 70$ to 7900) and comparison Mie extinction coefficients ($Q_{\rm ext} = 2.0$ to 2.1)—Mie particles in the geometric regime tend toward $Q_{\rm ext} = 2$ (B. Hapke 2012). We therefore compute the normalized phase function using the method of K. Muinonen et al. (2009), by first normalizing the measured, geometric phase curve $F_{11}^{\rm G}$ after applying zero-slope conditions at the ends. A separate, size-weighted Fraunhofer diffraction shape ($F_{11}^{\rm D}$) is then computed. For an assumed scattering coefficient $Q_{\rm sca}$, $F_{11}$ is then expressed as the weighted sum,

$$F_{11}(\alpha) = \frac{Q_{\rm sca} - 1}{Q_{\rm sca}} F_{11}^{\rm G}(\alpha) + \frac{1}{Q_{\rm sca}} F_{11}^{\rm D}(\alpha). \tag{13}$$

Attempts to estimate scattering efficiency of random Gaussian spheres over the same size distribution were carried out in two very similar studies by T. Nousiainen et al. (2011) and J. Escobar-Cerezo et al. (2017).

They used geometric optics with additional diffuse scattering effects applied to the host particles, referred to as Ray Optics with Diffuse Scattering (RODS) effects applied to the host particles. Diffuse scattering applied to the host particles produced estimates of single-scattering albedo ranging from 0.65 to 0.85 ($Q_{\rm sca} = 1.33$ to 1.74) by varying refractive index, concentration of internal and external scatterers (excluding

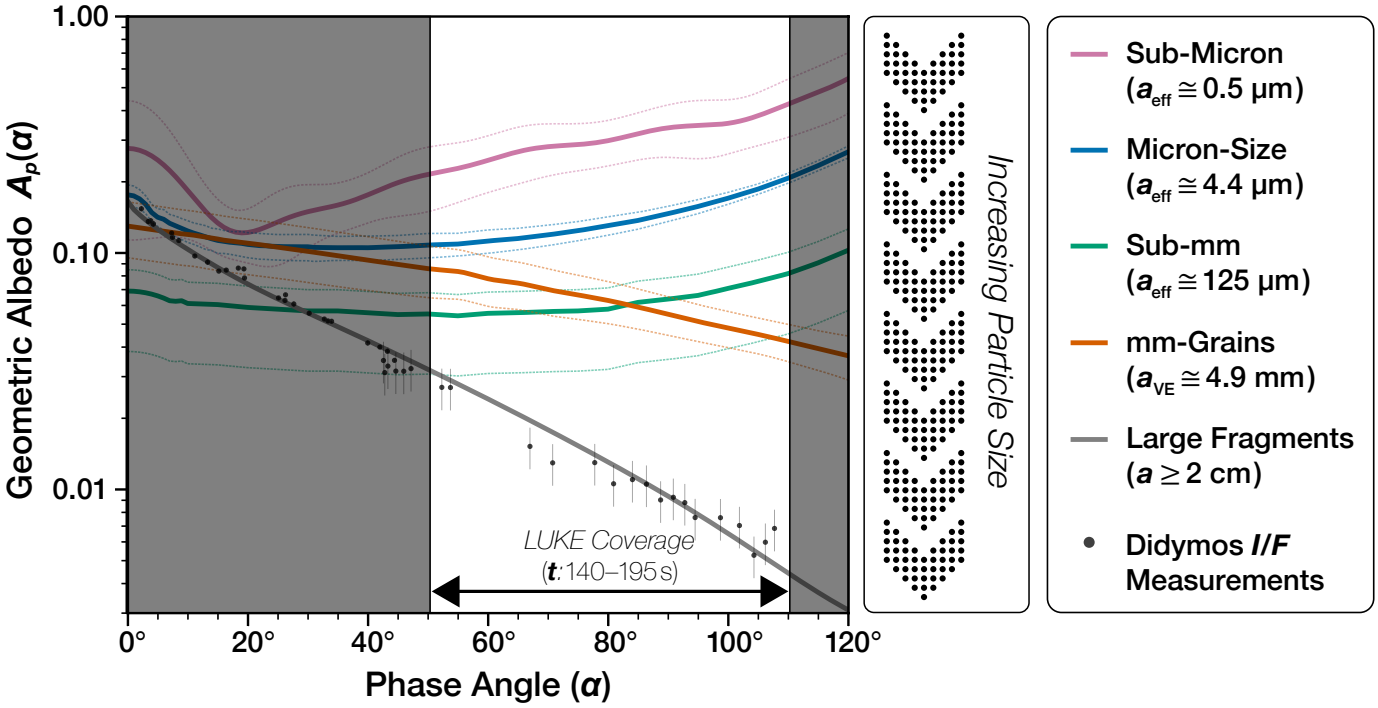


**Figure 8.** Phase curves showing geometric albedo in five grain size categories, derived from modeling, lab measurements, and observations. Radii listed for each category are the average values of its members, and bold lines show the average curves ($a_{VE}$ indicates volume-equivalent radius). Geometric albedo of small grains typically declines at small phase angles, then increases as a result of forward scattering, whereas *mm-Grains* and larger particles decrease monotonically in brightness with increasing phase angle. This fundamental change in scattering behavior occurs at particle radii of around 1 mm.

water ice), and properties of those scatterers. Figure 8 (bold line) shows the average albedo curve for a host particle with $Q_{sca} = 1.6$ (corresponding to $\mathrm{Im}(m) \approx 10^{-4}$). Fainter lines correspond to the extreme values of $Q_{sca}$. The albedo of these grains is observed to be lower than that of smaller particles, evidently due to the persistence of forward scattering and size-dependent absorption in the host particles. Some questions remain regarding the normalization of the phase function derived from this single measurement, and the resulting absolute scaling of the albedo curves for this size category. This can be traced to the general inability of RODS models to reproduce the measured $F_{11}$ shape. Additional large-grain measurements with coupled modeling would help to resolve these questions.

*millimeter-Grains*. The millimeter to centimeter size category represents the important transition from small particles consistent with forward scattering to large fragments with phase curves that decline in brightness with phase angle. Phase curve shapes for laboratory "pebbles" with spherical volume-equivalent radii ($a_{VE}$) from 1.5 to about 4 mm have been documented by laboratory measurements (O. Muñoz et al. 2017, 2020; E. Frattin et al. 2022). To estimate the absolute brightness of particles in this size range, we examine particles of similar size, naturally ejected from active asteroid Bennu, which were measured photometrically by C. W. Hergenrother et al. (2020) using the OSIRIS-Rex camera system. As described in Appendix C, we utilize measurements of a set of "best-observed" Bennu particles, and compare them with 520 nm laboratory measurements of porous (Etna) and more compact (MgFeAlSi) "pebbles," in order to obtain geometric albedo curves for these particles, after correcting for the very different albedos of the parent bodies (≈0.044 for Bennu versus 0.12 for Didymos, ignoring opposition brightening).

*Large Fragments*. This size category applies to plume fragments that are centimeter-sized and larger, and is represented by the phase curve of the Didymos-Dimorphos system itself. The curve (thick gray line) is constructed using basis functions in the $H$, $G_1$, $G_2$ photometric system as defined by K. Muinonen et al. (2010). Coefficients $G_1$, $G_2$ representing Didymos (0.73 and 0.17, respectively) were obtained by P. H. Hasselmann et al. (2024) using a combination of LICIACube and ground-based measurements. A zero-phase geometric albedo $A_{p0}$ of 0.165 brings this curve shape into best overall visual agreement with the measurements, illustrated by the overlying scatter plot with measurement uncertainties included.

### 3.2. Plume $I/\mathcal{F}$ and Phase Angle Dependence

Figure 9 shows plume $I/\mathcal{F}$ computed for a set of representative green channel images and reveals a dramatic decline in plume brightness with increasing phase angle (left to right). All images have been scaled to 7 m px$^{-1}$, and maximum $I/\mathcal{F}$ in each image is called out in the annotation. Points within the Dimorphos outline are set to zero so that only plume particles contribute to observed scattering. An oversize mask has been applied to the outline of Didymos (shown as a dotted outline) in each image in order to suppress correlated stray light. Using the albedo curves of Figure 8 and results of additional computations showing the differential size distributions of visible scattered light (see Figure 14 and the surrounding discussion), the observed brightness roll-off is found to be consistent with millimeter and somewhat larger (centimeter) grains dominating the scattered light at small and large phase angles, respectively. This conclusion is in broad agreement with estimated particle sizes from other modeling and observational studies: 200 $\mu$m (A. Penttilä et al. 2024),

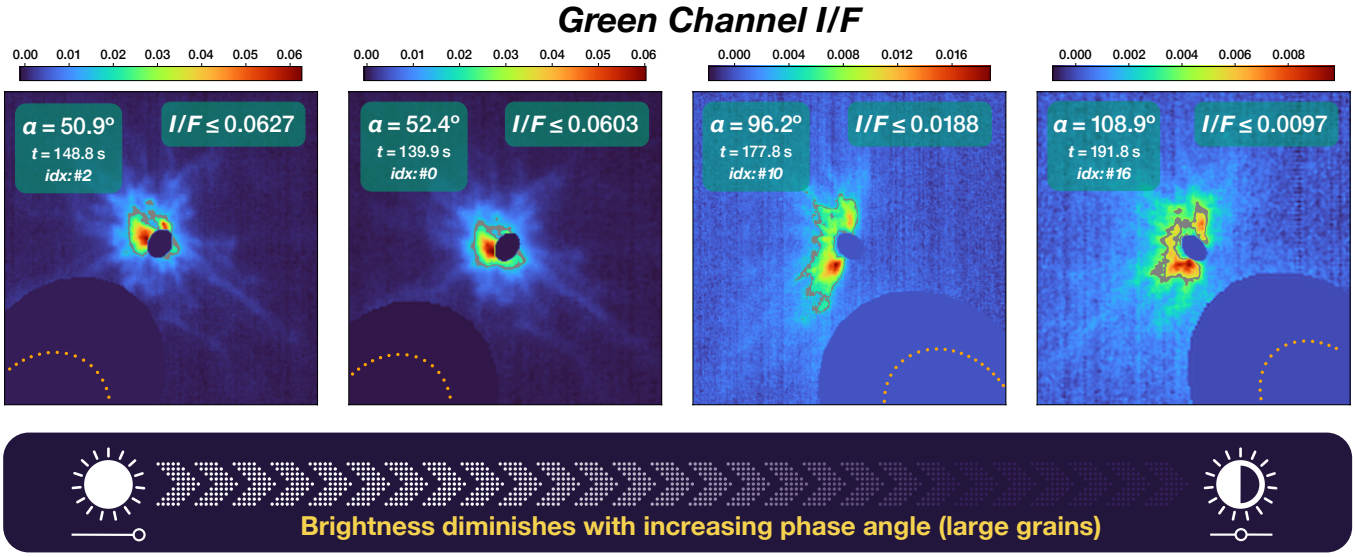


**Figure 9.** Sample $I/\mathcal{F}$ images showing the overall decrease in plume peak brightness (left to right) between small phase-angle measurements clustered between 50.°6 and 52.°9, and the large phase-angle images which span 94° to 110°. Dimorphos interior is set to zero, and Didymos outlines are shown dotted. Peak brightness in each plot is indicated in the annotation. The authors attribute the downward trend in brightness to the decline in albedo of millimeter to centimeter particles with increasing phase angle, as well as changing plume perspective during LICIACube flyby. There may also be some minor influence from a redistribution of plume optical density as particles flow outward from the impact site. Thin, gray zones indicate the transition between optically thin and thick regions ($\tau = 0.2$ to 0.25), albeit with large uncertainties.

submillimeter to millimeter (N. X. Roth et al. 2023), and millimeter to centimeter (Z.-Y. Lin et al. 2023).

By combining information in Figures 8 and 14, it is possible to approximate the location where the plume transitions from optically thin to thick, by noting that the brightness ($I/\mathcal{F}$) of a thin plume is $\tau A_p(a, \alpha)$, with $\tau$ the geometric optical depth. From Figure 8, we adopt a millimeter-grain value of $A_p \approx 0.08$ for measurements near $\alpha = 52°$. Near the largest phase angles ($\alpha = 105°$), we estimate a "centimeter grain" value of perhaps 0.02 for $A_p$, noting that uncertainties in these values can easily be a factor of 2 or more. A transition region defined by $\tau = 0.20$ to 0.25 is highlighted gray in the images. This transition range choice is based on the comparison of single- and multiple-scattering results for reflection and transmission cases that would be typical of the LICIACube flyby shown in Figure 3 of R. Lolachi et al. (2023b). These simulations showed that departures from the single-scattering case at $\tau = 0.2$ are significant. The locations and widths of these regions on the images also depend on the LICIACube LOS direction, as the spacecraft moves from a frontal view of the plume to a side view and eventually a backward looking perspective near the last time step. Quantitative relations between plume total brightness, mass, and observing geometry are defined in Section 4. Implications of the innermost, optically thick region for plume mass estimates are discussed further in Section 6.

One additional source of excess light not considered in the set of plume radiance corrections (Section 2.2) is added brightness observed at LICIACube due to indirect illumination of plume particles from the Didymos system. While a full treatment of this effect is well beyond the scope of this study, it was possible to make a coarse estimate by first estimating the Didymos flux on a test particle near Dimorphos (all flux was assumed to come from Didymos center), followed by its scattered radiance in the direction of LICIACube. The results, for all analog sizes up to millimeter-grains, showed that this added radiance is <1% of direct solar scattering (i.e., smaller than the uncertainties) and can therefore be reasonably ignored.

## 4. Radiance Models and Plume Mass Estimates

Plume mass and brightness can be related, since both depend on the size distribution and overall concentration of particles. Further, where the plume can be considered optically thin, the details of the plume geometry are (contextually) not important, and mass and brightness along each LOS are proportional, leading to straightforward relations between these quantities. We allow for the possibility of a broken power-law size distribution $dN/da \sim a^{k_{1,2}}$, with values of $k_1$ and $k_2$ near $-2.7$ and $-3.7$, derived from studies of the evolving tail by J.-Y. Li et al. (2023) and F. Moreno et al. (2023), although uncertainties as large as 0.2 accompany both observations. From those same authors, we adopt approximate size distribution limits $a_{\min}$, $a_{\max}$ and transition grain radius ($a_t$) of 1 $\mu$m, 5 cm, and 3 mm, respectively. Consistent with recent impact studies (S. D. Raducan et al. 2024), the mass density of individual particles, $\rho$, is taken to be 3500 kg m$^{-3}$ (i.e., specific gravity of 3.5; W. D. I. Carrier et al. 1991) as Dimorphos is an S-type asteroid with the best-matching meteorite analogs being L/LL chondrites with grain densities ranging $\approx$3200 to 3600 kg m$^{-3}$ (J. de León et al. 2006; T. L. Dunn et al. 2013; S. Ieva et al. 2022; D. Polishook et al. 2023).

The relation between predicted, or model, radiant intensity in each RGB color channel, and plume mass $M$ within the LUKE FOV (see the complete derivation in Appendix B) becomes

$$I_{\rm mdl}(\alpha, a_j, k_{1,2}) = \frac{\bar{J}_\odot}{\pi}\frac{3}{4\rho}\frac{S_I(\alpha, a_j, k_{1,2})}{S_M(a_j, k_{1,2})}M. \quad (14)$$

with $a_j$ indicating the reference radii defining the size distribution ($a_j = a_{\min}, a_t, a_{\max}$). Mass factor $S_M$ is obtained

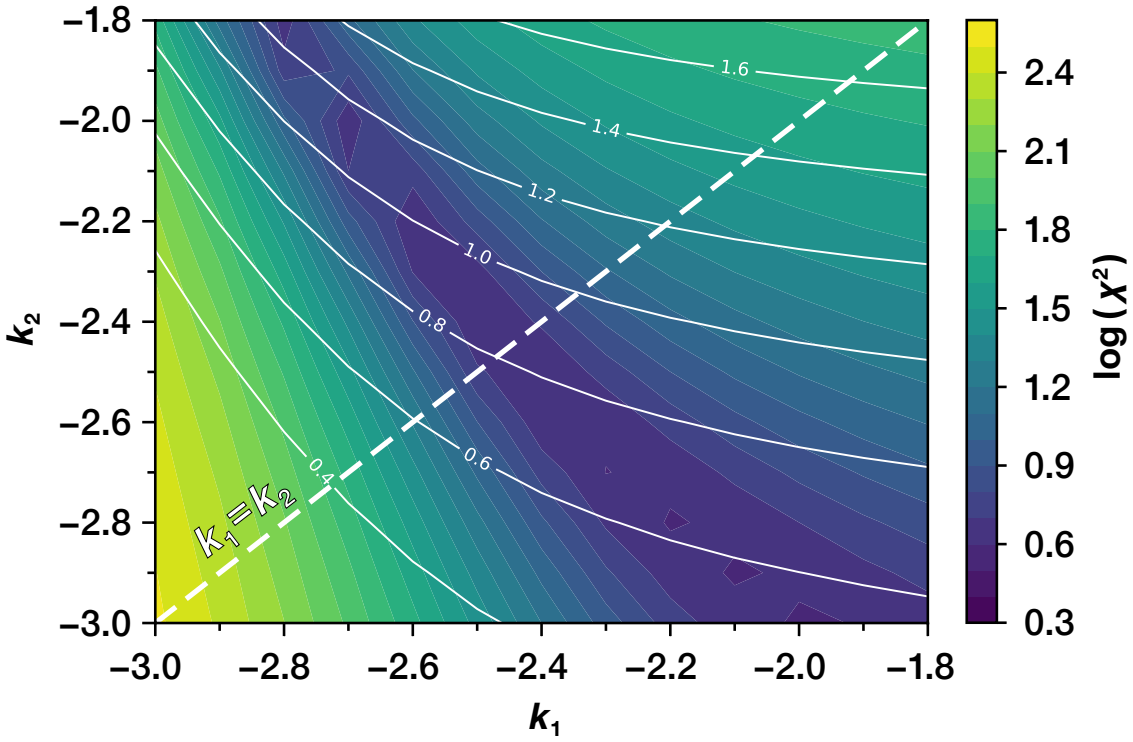


**Figure 10.** Map showing degree of agreement (objective function) between LICIACube measurements of plume intensity in the green channel and model predictions, expressed as $\chi^2$ (see the text for definition). Smaller values (darker regions) represent better agreement. White contours indicate plume mass in units of $10^7$ kg. Particle mass density used in the models is $\rho = 3500$ kg m$^{-3}$, and size distribution parameters $a_{\rm min}$, $a_{\rm t}$, and $a_{\rm max}$ are fixed at 1.0 $\mu$m, 3.0 mm, and 5.0 cm, respectively. No single minimum in $\chi^2$, hence no unique $k_1$, $k_2$ solution appears in the plot, indicating that visible-band measurements alone cannot provide information on the size distribution when those populations are spatially overlapping. However, a single coefficient solution ($k_1 = k_2$, white dashed line) follows a path of steepest descent, reaching a minimum at $k = -2.4$ and plume mass of $\approx 8.5 \times 10^6$ kg.

by straightforward integration,

$$S_M(a_j, k_{1,2}) = \left(\frac{a_{\rm t}^{k_1+4} - a_{\rm min}^{k_1+4}}{k_1+4}\right) + a_{\rm t}^{k_1-k_2}\left(\frac{a_{\rm max}^{k_2+4} - a_{\rm t}^{k_2+4}}{k_2+4}\right), \quad (15)$$

while intensity factor $S_I$ is computed by numerically integrating along the $A_p(a, \alpha)$ surface,

$$S_I(\alpha, a_j, k_{1,2}) = \int_{a_{\rm min}}^{a_{\rm t}} A_p(a, \alpha)\, a^{k_1+2} da + a_{\rm t}^{k_1-k_2} \int_{a_{\rm t}}^{a_{\rm max}} A_p(a, \alpha)\, a^{k_2+2} da, \quad (16)$$

using the reference radii listed in Figure 8 as nodes. Intermediate points are obtained by linear interpolation in $\alpha$ and logarithmic interpolation in particle radius. Values of $A_p(>2\,{\rm cm})$ are set equal to $A_p(2\,{\rm cm})$.

We further examined the possibility that the LICIACube images show a single (versus broken) power-law coefficient by comparing measured radiances in the green channel, as shown in Figure 6, with intensity predictions from Equation (14), in the form of a goodness-of-fit ($\chi^2$) map. Defining $N_{\rm im}$ as the total number of valid images ($N_{\rm im} = 12$), Figure 10 shows the $k_1$, $k_2$ objective function, defined as

$$\chi^2(k_1, k_2) = \frac{1}{N_{\rm im}} \sum_{i=1}^{N_{\rm im}} \frac{[I(\alpha_i) - I_{\rm mdl}(\alpha_i, k_1, k_2, M)]^2}{I_{\rm mdl}(\alpha_i, k_1, k_2, M)}, \quad (17)$$

where the darkest region represents best agreement. The influence of changing mass at each $k_1$, $k_2$ point is corrected for by adjusting $M$ to equate the averages of measurement and model. It is apparent that, while two size populations may exist in the nascent plume observed by LICIACube, they cannot be distinguished when they are spatially mixed, although the elongated zone of best agreement suggests a linear relationship between $k_1$, and $k_2$. We note that this zone lies in a direction nearly orthogonal to a single-$k$ ($k_1 = k_2 = k$) power-law relation, shown as the white dashed line in Figure 10. This line therefore follows a path of steepest descent, with a well-defined minimum at $k = -2.4$ and corresponding plume mass of $\approx 8.5 \times 10^{-6}$ kg. This $k$-value is slightly less steep than $-2.5$ and $-2.7$ estimated for the small grain component ($k_1$) of the more evolved plume, from ground-based and HST measurements (J.-Y. Li et al. 2023; F. Moreno et al. 2023).

### 4.1. Mass Retrievals

Under the assumption of a single power law, we separately retrieved R, G, and B estimates of plume mass and $k$ using a similar goodness-of-fit comparison between error-weighted measurements and models, as shown in the left-hand set of the Figure 11 panels. The plots show contours of constant log $\chi^2$, where now,

$$\chi^2(M, k) = \sum_{i=1}^{N_{\rm im}} \frac{w_i [I(\alpha_i) - I_{\rm mdl}(\alpha_i, k, M)]^2}{I_{\rm mdl}(\alpha_i, k, M)}, \quad (18)$$

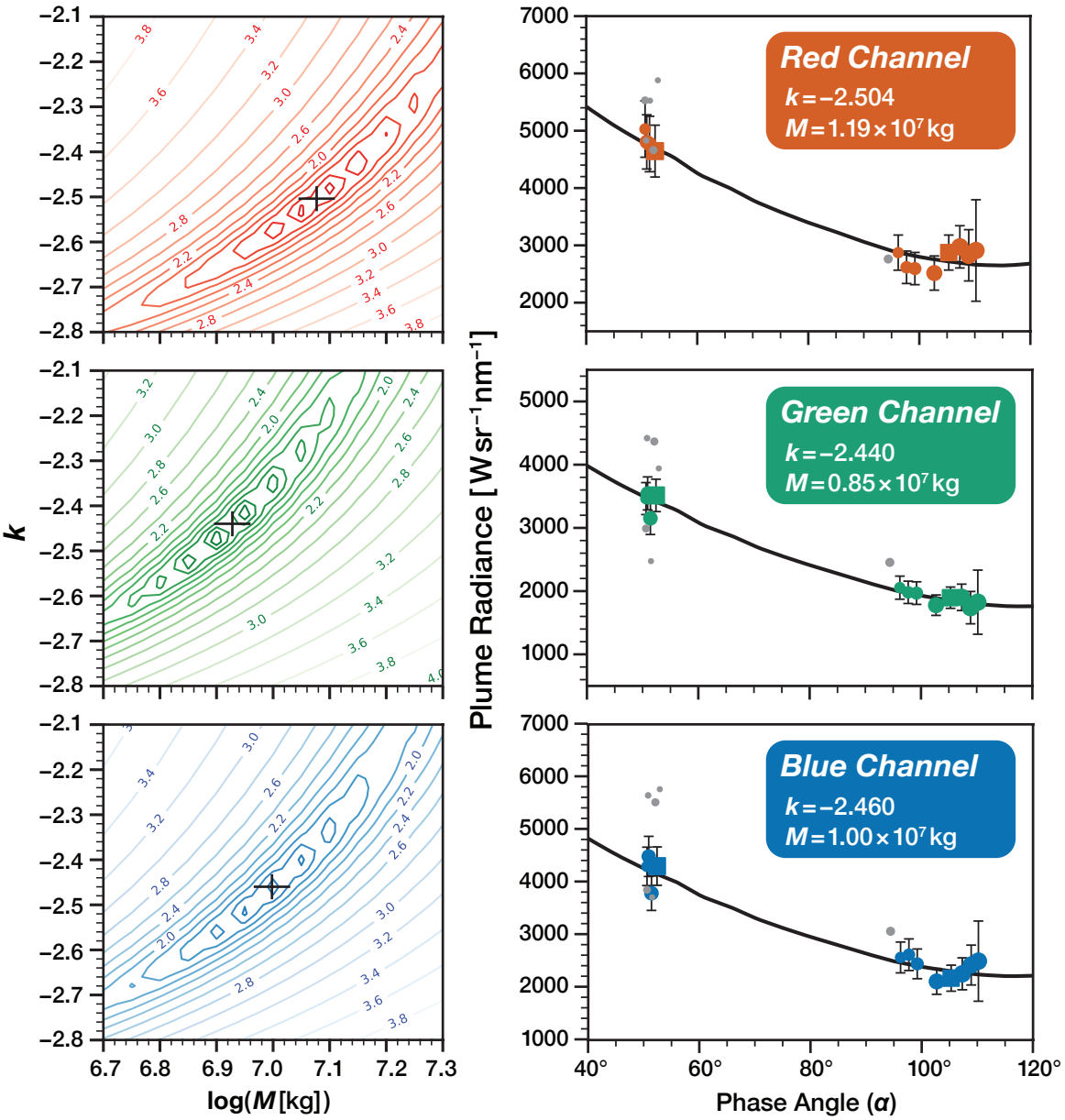


**Figure 11.** Estimates of plume mass in the R, G, and B channels, determined by mapping the goodness of fit between error-weighted measurements $I$ and models $I_{\rm mdl}(M, k)$. The left panels show contour plots of $\log(\chi^2)$ as described in the text. Smaller values represent better agreement, and unique solutions (located by inspection) lie at the positions of the crosshairs. Other model parameters are as stated in Figure 10. The right panels show the corresponding best-fit models overlaid with the data points. Sources of systematic error obtained from the responsivity calibration (Section 2.1) are not included in the weighting or in the data error bars. As in Figure 6, target distance is proportional to symbol size, squares indicate reference images from Table 1, and gray symbols are "heavily clipped" images excluded from the analysis.

with measurement weights

$$w_i = \left[\Delta I_i \sum_i \left(\frac{1}{\Delta I_i}\right)\right]^{-1}. \quad (19)$$

Log quantities are used in order to visualize the entire search space and ensure that a global $\chi^2$ minimum is identified. Crosshairs in each map show the minimum values over the map domain, as judged by the overall symmetry of the contours. This visual centering method carries an uncertainty of perhaps 0.03 in $\Delta\log(M)$, or 7% in $M$.

The right panels show the resulting models overlaid with the scatter plots. Values of retrieved mass range from 0.85 to $1.19 \times 10^7$ kg, with $k$ more tightly constrained between −2.45 and −2.50. The reason for the large (35%) spread in mass estimates is not obvious, but may lie with the responsivity calibration, with uncertainties as large as 26% in the blue channel (Section 2.1 and Appendix A). To the extent that RGB responsivity errors are independent, mass estimates could shift in opposite directions and deviate by this amount. As a result, any systematic trends resulting from changing plume color with radial distance, or LICIACube perspective, could be easily masked. Another error source may lie in the RGB filter response shapes if they are not known accurately, especially in the red leak and blue leak extensions. These can influence the results, since color-temperatures of the calibration stars differ from that of the plume. It is also quite likely that the particle albedo map $A_p(a, \alpha)$ includes a color dependence. We were not

able to account for this due to the limited sample size making up the particle albedo data (Section 3).

## 5. The Influence of Optical Depth on Plume Mass Estimates

In the case of at least one image, it was possible to estimate additional mass near plume center not accounted for in the single-scattering approximation, by extrapolating the trend in areal mass concentration $m$ (kg m$^{-2}$) as lines of sight approach Dimorphos. We used Image #0 ($\alpha_0 = 52.^{\circ}4$), green channel data for this estimate because of its generally large SNR and wide spatial coverage. Because of the observing geometry, the plume lies in front of Dimorphos and is observed to be optically thick over at least a portion of its surface area.

The needed single-scattering relations are described in Appendix B. Measured specific intensity $I$ (W m$^{-2}$ sr$^{-1}$ nm$^{-1}$) is converted to areal mass concentration $m$ (kg m$^{-2}$) along each LOS,

$$m = \frac{\pi}{\bar{J}_{\odot,\mathrm{R,G,B}}} \frac{4\rho}{3} \frac{S_M}{S_I} I_{\mathrm{R,G,B}}, \tag{20}$$

with $\bar{J}_{\odot,\mathrm{R,G,B}} = 1.65,\ 1.86,$ and $1.87$ W m$^{-2}$ nm$^{-1}$, respectively. As discussed in Section 4, the LICIACube image data implies that the early plume can be described by a single power law. Using our assumed particle size limits of $a_{\min} = 1$ $\mu$m and $a_{\max}$=5 cm (the choice of $a_{\min}$ has little influence), and power law $k = -2.44$ for the green channel, the mass factor $S_M(a_{\min}, a_{\max}, k)$ simplifies to a single scale factor that is applied to the entire image,

$$S_M = \frac{a_{\max}^{k+4} - a_{\min}^{k+4}}{k+4} = 5.99 \times 10^{-3}. \tag{21}$$

Further, at constant $\alpha_0 = 52.^{\circ}4$, numerical integration of $A_p(a, \alpha_0)$ follows a single path along the albedo surface, and the intensity factor $S_I(\alpha, a_{\min}, a_{\max}, k)$ simplifies to

$$S_I = \int_{a_{\min}}^{a_{\max}} A_p(a, \alpha_0)\, a^{k+2}\, da = 0.189. \tag{22}$$

A similar relation can be constructed for optical depth, which has the same particle size dependence as intensity,

$$\tau = \frac{S_\tau}{S_I} \frac{\pi}{\bar{J}_\odot} \tag{23}$$

with

$$S_\tau = \frac{a_{\max}^{k+3} - a_{\min}^{k+3}}{k+3} = 0.333. \tag{24}$$

As previously stated, radiance factor $I/\mathcal{F}$, is defined as $I/\mathcal{F} = (\pi/\bar{J}_\odot)I$.

Figure 12(A) shows a map of mass concentration derived from the green channel intensity image. Analogous to $\overline{I_{\mathrm{ring}}}(r)$ in Section 2.2, azimuthally averaged mass values $\bar{m}(r)$ (kg m$^{-2}$) are computed over contiguous narrow rings (1 pixel width in this case) extending from the outer boundary at $0.9\, r_b$ to the center. Didymos zero mask points are excluded from the averaging. Ring contributions $2\pi\, r\, \bar{m}(r)\, \Delta r$ are then accumulated from the outside boundary inward to define cumulative plume mass $M(r)$. Values of $\bar{m}(r)$ are shown mirrored about the radial distance axis in the lower panel. Azimuthal averaging yields a dramatic improvement in sensitivity compared with single-pixel values along the central row (gray line), at the expense of losing one spatial axis. In this example, ring contributions to plume mass begin to be observable about 2 km from the center. The optical depth profile (red), shows that the plume remains optically thin to within ≈200 m of center, but increases quickly at smaller distance. While some of the increase in brightness comes from Dimorphos, its contribution is expected to be small, since the portion not screened has a physical albedo of ≈0.03 at this phase angle (Figure 8).

A log–log plot of ring mass density $\bar{m}$ versus radial distance $r$, is shown in Figure 13(A). The log scale emphasizes the region near the image center, highlighting both the Dimorphos boundary and the LUKE, 2-pixel, spatial resolution limit shown as a gray band. Over the optically thin portion of the data set ($\tau < 0.20$), Dimorphos has negligible influence on the scattered light. This portion of the plot reveals a surprisingly linear $\log(m) - \log(r)$ relation. By extending this trend to within 2 pixels (≈26 m) of Dimorphos center using a three-point straight line fit, $\log \bar{m}(r) = c_1 + c_0 \log r$ with $c_0 = -2.185$ and $c_1 = 6.139$, we compute an augmented estimate for plume mass. Assigning a zero-point distance $r_0$ at $\tau = 0.1$ with corresponding $M_0$, the revised mass is obtained by adding discrete ring contributions to $M_0$,

$$M = 2\pi\ 10^{c_1}\, \Delta r \sum_{r_0}^{r=0} r_i^{1+c_0} + M_0. \tag{25}$$

The red line in Figure 13(B) shows the enhanced plume mass defined by the linear extrapolation. This revised value of mass amounts to a substantial increase (≈77%) over the single-scattering estimate (black line). Shaded portions represent the statistical measurement uncertainty of 7% as defined in Section 2.4 (dark band) and the added calibration uncertainty of 13% in the green channel (lighter band).

We consider this empirical result, with added uncertainties, to be a plausible upper limit for the fractional increase in mass in the optically thick inner plume region, although it has been carried out for only one image and one color channel. A more comprehensive treatment would incorporate a knowledge of the 3D plume and observing geometries (J. D. P. Deshapriya et al. 2023; M. Hirabayashi et al. 2025), which we have not explored, as well as a multiple-scattering code that relates measured brightness to path abundance (m$^{-2}$) along each LOS. Such an analysis is well beyond the scope of this study.

## 6. Discussion

It is worth comparing the mass and radiance estimates derived here with plume characteristics documented from ground-based and HST observations. An initial release of very fast ejecta material associated with a large brightness change at the time of impact was observed from several ground-based telescopes (A. Fitzsimmons et al. 2023; A. Graykowski et al. 2023; L. Shestakova et al. 2023) and also by the Lucy spacecraft (H. A. Weaver et al. 2024). A near-instantaneous brightness change of ≈2.3 mag in the Johnson $V$ band was recorded by a small telescope network (A. Graykowski et al. 2023), with field-stop equivalent to 750 km at the Earth-asteroid distance of 0.076 au (at impact time). Applying the Johnson magnitude-flux conversion (see Appendix A), this corresponds to a maximum plume brightness of $\approx 5.7 \times 10^4$ W sr$^{-1}$ nm$^{-1}$. Over a period of ≈15 minutes,

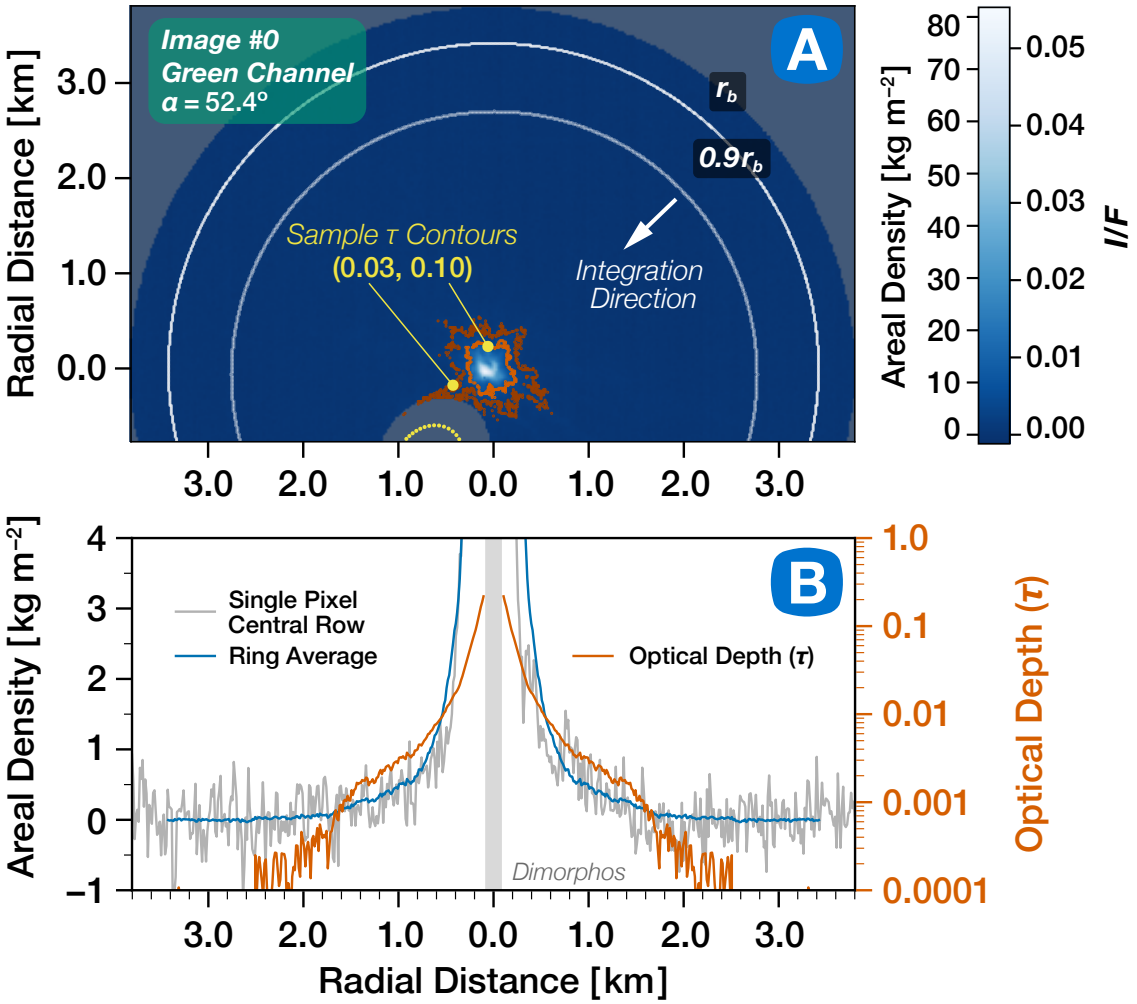


**Figure 12.** Panel (A): map showing plume areal mass density $m$ (kg m$^{-2}$) and brightness ($I/\mathcal{F}$), obtained from measured Image #0. Azimuthal averages of mass density $\bar{m}(r)$ are computed in narrow rings extending from the outer boundary at 0.9 $r_b$, inward to $r = 0$. Optically thick scattering occurs within the $\tau = 0.1$ contour outlined in red. Panel (B): gray plot shows the noise resulting from single-pixel sampling along the central image row, while the blue line shows vastly improved sensitivity that results from azimuthal averaging in contiguous 1 pixel-wide rings (excluding the Didymos zero mask). Ring average ($\bar{m}$) and optical depth profiles are shown mirrored around $r = 0$.

brightness then declined and stabilized at about $2.1 \times 10^4$ W sr$^{-1}$ nm$^{-1}$, indicating that a large initial burst of small dust particles, including some atomic species (likely released from the dust; L. Shestakova et al. 2023), exited the FOV at up to $\approx$2 km s$^{-1}$. Including the other observations, estimates of the ejecta velocity range from 1 to 3.6 km s$^{-1}$. Given the high velocities, this very fast ejecta will have left the LICIACube FOV before the observations used for this study. Mass estimates for this high-speed component range from $\sim 10^2$ to $10^3$ kg (A. Fitzsimmons et al. 2023; A. Graykowski et al. 2023; H. A. Weaver et al. 2024), amounting to $<$1% of the mass inferred from our LICIACube results ($1.6 \times 10^7 \pm 0.3 \times 10^7$ kg).

Using a combination of ground-based and HST measurements, F. Moreno et al. (2023) modeled the ejecta evolution from days to months after the impact. For the ground-based measurements, they used a "simple" Monte Carlo (MC) analysis where they injected ejecta outside the Hill sphere of the Didymos-Dimorphos system and tracked the Keplerian motion of particles under the influence of solar gravity and radiation pressure only. Ejecta from the initial impact was injected into the model using both a fast conical release (corresponding to the ejecta cone of the impact, and not the same as the very fast ejecta discussed above) and a slower hemispherical release. The model determined that the total unbounded ejecta used to form a tail was $0.42 \times 10^7$ kg. For the HST measurements, a more complex "detailed" MC model with the same injection methods was implemented that started ejecta within the binary system and took into account the gravitational interactions of the particles with the asteroids, as well as the other forces. The unbound ejecta mass in this approach was $0.49 \times 10^7$ kg, while the total ejecta lower limit released from the impact was $>0.6 \times 10^7$ kg. This was deemed a lower limit due to the difficulty in accounting for the boulder mass contribution. It should also be mentioned that F. Moreno et al. (2023) used a broken power-law size distribution for their final results ($k_1 = -2.5$ for particles of $r \leqslant 3$ mm and $k_2 = 3.7$), as it resulted in a better match in tail morphology between model and observations. A single unbroken power law would have yielded higher mass estimates. As their observations started days after impact, the resulting broken power-law ejecta size distribution is likely the result of size-sorting driven by SRP. This would explain why their mass estimate is significantly lower than ours, with an unbroken power-law size distribution.

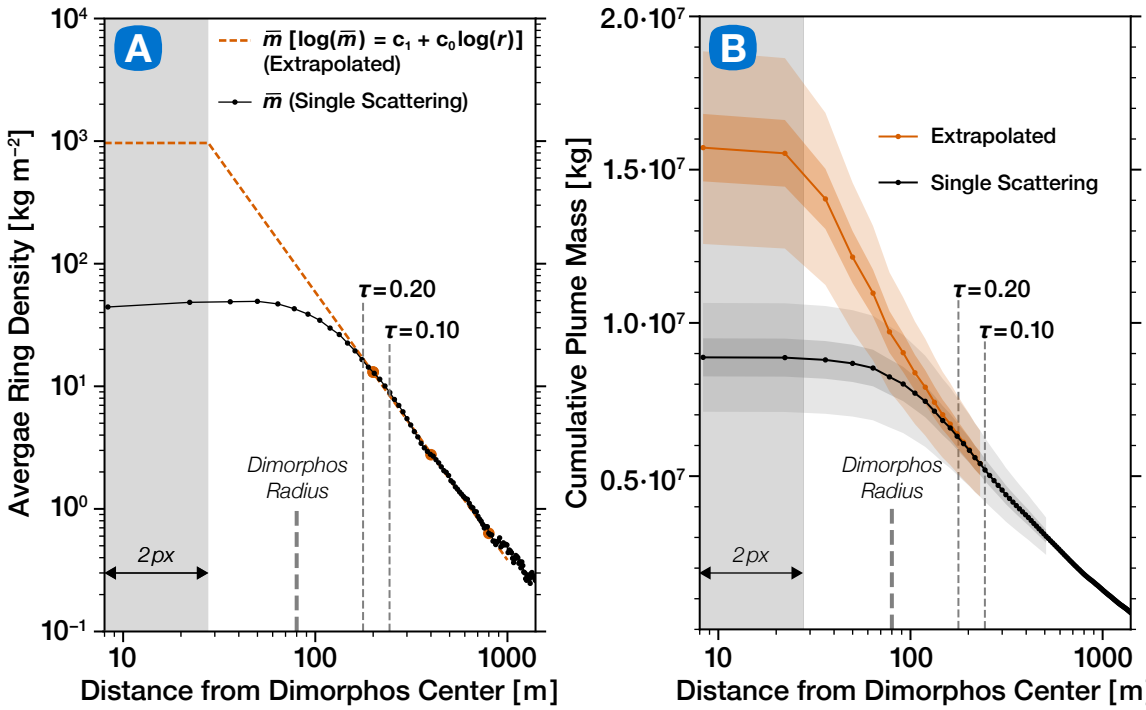


**Figure 13.** Panel (A): log–log plot showing mass density estimated by single-scattering (black line) vs. distance from center. Black dots indicate ring outer boundaries. Within the region of high SNR and small optical depth ($\tau < 0.2$), the plot shows a remarkably linear relation, leading to an empirical extrapolation of plume mass density to near center as determined by a three-point linear fit (red dots). The gray area at the left indicates the 2 px (resolution) limit. Panel (B): cumulative plume mass, extending to center. The extrapolated curve shows the projected mass enhancement from the optically thick inner plume region. Darker shading represents the statistical uncertainty in the derived intensities (Section 2.4) and lighter shading the added calibration uncertainty described in Section 2.1 and Appendix A.

To allow for a more thorough comparison with our mass results, it is worth looking in more depth at the fast conical and slow hemispherical mass components in the detailed MC (HST) model. The fast conical component has a mass of $0.21 \times 10^7$ kg, comparable with our mass estimates. The inferred size–speed distribution showed that grain radii less than a few tens of microns would have been depleted within ≈3.5 km radius LUKE FOV during the period of observation. This raises the possibility that we may have missed some ejecta in our study. This size range, however, amounts to an extremely small fraction of this plume mass component, which is dominated by much larger (submillimeter to centimeter) particles moving at a few meters per second (see Figure 14).

The second, hemispherical slow component with velocity $\lessapprox$0.1 m s$^{-1}$ has an even larger mass of $0.43 \times 10^7$ kg. Within the first few minutes from impact, this portion would have been indistinguishable from Dimorphos and therefore not observed by LUKE. We presume this to coincide with the optically thick portion of the plume described in Section 3, and discussed further in Section 5. Performing a simple order-of-magnitude check using the values from Table 1 shows that projected ejecta speeds in the image plane ($r_b/t$ are ≈2 to 27 m s$^{-1}$). This lower limit, consistent with the slower speed ejecta (∼m s$^{-1}$) seen in these other observations, arises when the 3D plume geometry is not considered. A more accurate analysis of ejecta speeds, tracking individual features within the ejecta, was performed by E. Dotto et al. (2024). Using LICIACube images from $t = 106$ to 118 s (earlier than those used in this study starting at $t = 140$ s), they found projected ejecta velocities ranging from 20 to 75 m s$^{-1}$, with some features reaching speeds of ≈500 m s$^{-1}$.

Early ($t = 5$ hr) HST observations of the plume over a much smaller (11 km diameter) area, though still larger than the LUKE FOV, showed a brightening of ∼1.0 mag, or $1.2 \times 10^4$ W sr$^{-1}$ nm$^{-1}$ (J.-Y. Li et al. 2023; Appendix A). These observations are consistent with a newly formed but extended plume, where total captured light increases with the size of the FOV. We point out that the contribution of Dimorphos to the total visible light ranges from zero to at most a few percent, depending on the optical depth of the occulting plume. Dimorphos is spatially separated from the plume in the later images.

Figure 14 provides some insight into the relation between brightness, mass, and size distribution. It shows the differential distributions of mass (Equation (B13)) and LUKE green channel brightness (Equation (B20)) as a function of particle size for a plume mass of $1.0 \times 10^7$ kg and single power-law ($k = -2.5$) size distribution. Constant phase-angle curves (53° and 110°) in the figure are representative of the LUKE image data. The smaller phase-angle value, which is approximately that of the ground-based and HST observations, is more sensitive to the concentration of larger grains. Grains smaller than ≈ 1 mm radius contribute a negligible amount to plume mass. However, at a fixed phase angle, a wide range of grain sizes, including those that contribute to plume mass, also contribute to the brightness. It is also worth noting how different these results are when compared with the constant $A_p$ curve (isotropic scattering) and how using this curve could lead to very different mass when used in a retrieval due to the overly large brightness contribution at larger particle sizes, a significant finding that was demonstrated in R. Lolachi et al. (2023a).

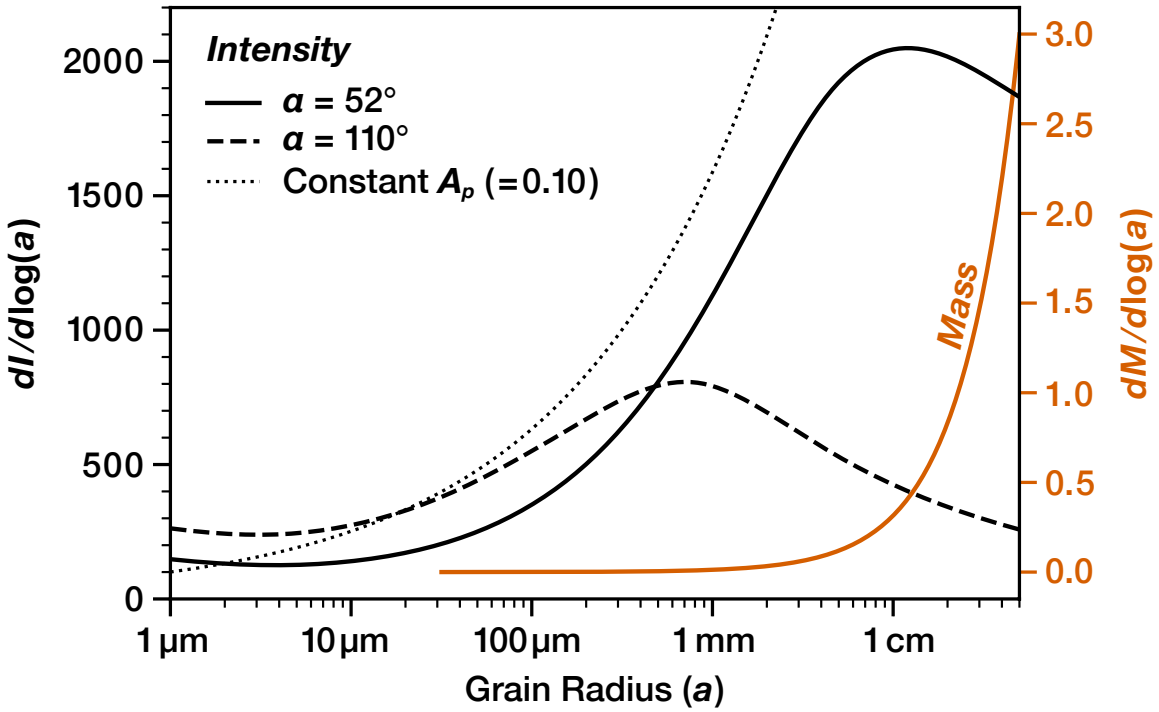


**Figure 14.** Differential intensity (calculated using Equation (14)) and mass relations for a single power-law ($k = -2.5$) size distribution and plume mass of $1 \times 10^7$ kg (see Figure 11, green). Grain sizes contributing to the observed scattering are strongly controlled by the size and phase-angle dependence of particle albedo. A constant albedo model ($A_p = 0.10$) is included for comparison.

For a fixed measured radiance, the retrieved mass, as in Figure 11, has only a modest dependence on the choice of $a_{\min}$, which is easily verified by adjusting $a_{\min}$ in the ratio $S_M/S_I(\alpha)$. Numerical tests show that increasing $a_{\min}$ from 1 $\mu$m to 50 $\mu$m, leads to a 25% increase in inferred mass at $\alpha = 110°$, but only 7% at 53°. Applying the same tests to $a_{\max}$ show that retrieved mass is roughly proportional to the assumed $a_{\max}$. Our mass retrievals, therefore, must rely on independent estimates of this parameter (e.g., F. Moreno et al. 2023).

Based on a single pre-CA observation with good image quality (Image #0, Section 5), we were able to estimate additional mass hidden in the central, optically thick portion of the plume by following the trend in areal mass density to image center. Significant optical depth also appears in post-CA images, but at lower SNR. The authors acknowledge that a similar trend analysis applied to all images, which we have not attempted, could lead to a different set of derived $k$-values, and possibly a further adjustment of plume mass.

### 6.1. Mass Estimate Comparison and Cohesive Strength Constraints

Table 2 compares mass estimates from this study with the work of others derived from modeling and/or observations (HST/ground-based). All plume mass results are broadly comparable after taking into account the diversity of approaches and boundary conditions in these studies, particularly FOV and assumed upper limit for fragment size. Of note is the large range (1.3 to 6.4 $\times 10^7$ kg) seen in the results from the Atacama Large Millimeter/submillimeter Array (ALMA) and the Atacama Compact Array (ACA) of N. X. Roth et al. (2023). This was due to assumptions made about the scattering material, with the lower- and higher-mass values calculated for amorphous and crystalline silicates, respectively. A large range, 1.1 to 5.5 $\times 10^7$ kg, was also found in F. Ferrari et al. (2025), who compared synthetic images generated with dynamical models to HST images. This was mainly due to uncertainties regarding the unresolved ejecta material near Dimorphos in HST images. They determined a best-fit mass of $1.9 \times 10^7$ kg, likely a lower limit due to the unknown population of larger, unconstrained ejecta particles that remain bound to the Didymos system.

A special subset of the ejecta worth further discussion is the population of ejected boulders (D. Jewitt et al. 2023; T. L. Farnham et al. 2025). This is because the boulders are likely to contribute a large fraction of the ejected mass, but contribute a far smaller fraction of the scattered light. This means they are much harder to detect due to being much darker scatterers (see Figures 8 and 14); consequently, their mass contribution is harder to measure, and hence measurements of boulder mass are lower limits. Additionally, for the boulder results cited in Table 2, an assumed density of 2200 to 2400 kg m$^{-3}$ is used, the value of or close to the Dimorphos bulk density. This is likely too low, as the asteroid bulk density takes into account void spaces present within the asteroid, whereas a boulder is more likely to be a monolithic object. Consequently, these mass estimates could be revised upward by 46% to 60% using a density of 3500 kg m$^{-3}$, consistent with S-type asteroid material, as discussed in Section 4.

As mentioned in Section 1, knowledge of ejecta mass provides constraints on asteroid strength and porosity. A. F. Cheng et al. (2024) compared uncalibrated LICIACube images with optical depth derived from point-source scaling models using the scaling relations of K. R. Housen & K. A. Holsapple (2011) and numerical impact simulations of S. D. Raducan et al. (2024). Their results quantified the relationship between ejecta mass and cohesive strength, for strengths varying from 5 to 5000 Pa (shown in Table 1 of their paper). Lower strength values imply an impact in the gravity-

**Table 2**
Comparison of Mass Estimates from Other Studies with This One.

| Study | Description | FOV[a] (km) | Mass Estimate ($M$) (kg) |
|---|---|---|---|
| This Study | RGB LUKE FOV Retrievals (optically thin plume portion) | $\geqslant 6 \times 6$ | $0.85–1.19 \times 10^7$ |
| | Total Mass: Inc. extrapolation (optically thin + optically thick plume portion) | | $1.6 \times 10^7 \pm 0.3 \times 10^7$ |
| N. X. Roth et al. (2023) | ALMA/ACA Observations | $r \geqslant 50$ | $1.3–6.4 \times 10^7$ |
| A. Graykowski et al. (2023) | Ground-based citizen scientists' telescopes | $r = 75$ | $1.3 \pm 0.1 \times 10^7$ |
| Y. Kim & D. Jewitt (2023) | Models of HST Observations: Particles (1 $\mu$ to 20 cm) | $\geqslant 1580 \times 580$ | $1.7 \times 10^7$ |
| | Including boulders (1 $\mu$ to 3.5 m) | | $2.2 \times 10^7$ |
| D. Jewitt et al. (2023) | HST Boulder Observations (Assumed $\rho = 2200\ \mathrm{kg\ m^{-3}}$) | $12700 \times 7700$ | $0.5 \times 10^7$ |
| T. L. Farnham et al. (2025) | LICIACube Boulder Observations (Assumed $\rho = 2400\ \mathrm{kg\ m^{-3}}$) | $\geqslant 12 \times 7$ | $0.1 \times 10^7$ |
| F. Moreno et al. (2023) | Monte Carlo Models coupled with HST data (1 $\mu$m to 5 cm) | $\geqslant 733 \times 400$ | $>0.6 \times 10^7$ |
| F. Ferrari et al. (2025) | Dynamical models used to generate synthetic HST images with model-HST comparison | $\geqslant 864 \times 864$ | $1.1–5.5 \times 10^7$, Best-Fit: $1.9 \times 10^7$ |

**Note.**
[a] FOV indicates field of view for a given analysis projected onto the sky-plane at Dimorphos in kilometers. These are either rectangular or circular. For a rectangular FOV, dimensions are givens as $x \times y$. For a circular FOV, $r$ indicates radius used for aperture photometry. Where a "$\geqslant$" is given, this indicates the smallest FOV used in the analysis.

controlled regime with higher resulting ejecta masses, while higher strengths imply an impact in the strength-controlled regime with lower resulting ejecta mass. They also showed a relationship between ejecta optical depth and asteroid cohesive strength, with stronger cases showing lower optical depths near the impact location. This is due to detachment of the plume from the surface in high-strength cases, resulting in a clearing of opacity just above the impact region (K. R. Housen & K. A. Holsapple 2011; A. F. Cheng et al. 2024). Plume detachment occurs because crater growth in late-stage evolution is impeded by higher target strengths (K. R. Housen & K. A. Holsapple 2011; A. F. Cheng et al. 2024). In the gravity-regime, crater growth is not impeded, so there is no plume detachment, and hence no clearing of opacity.

Constraints on the cohesive strength, $Y$, of Dimorphos are informed by a comparison of our mass results with Table 1 from A. F. Cheng et al. (2024). For $M(Y = 5000\ \mathrm{Pa})$, a mass of $0.14 \times 10^7$ kg is given; this is much lower than even the low end of our single-scattering estimate of $M = 0.85 \times 10^7$ kg. Consequently, we can state that Dimorphos has $Y < 5000$ Pa. For $M(Y = 500\ \mathrm{Pa}) = 0.65 \times 10^7$ kg, the value is now comparable to our single-scattering estimate, though if we add the extrapolation for the optically thick inner region, at $M = 1.6 \pm 0.3 \times 10^7$ kg, this makes it look more likely that $Y < 500$ Pa. For $M(Y = 50\ \mathrm{Pa}) = 2.34 \times 10^7$ kg, we achieve the closest match, especially if we also add a boulder contribution. Including the D. Jewitt et al. (2023) boulder contribution, our mass estimate now increases to a possible maximum of $2.4 \times 10^7$ kg, very similar to $M(Y = 50\ \mathrm{Pa})$ value, implying $Y \leqslant 50$ Pa. We state this as a lower limit because it is quite possible that the total ejecta mass is higher given that our analysis was restricted to the near-field LUKE FOV, an unseen boulder contribution (as discussed above), and that the release of ejecta may not have completed before the end of LICIACube observations. This last point is suggested by the ongoing release of ejecta at the time of closest approach of $t = 167$ s (J. D. P. Deshapriya et al. 2023; E. Dotto et al. 2024) and results from M. Hirabayashi et al. (2022) that suggest a crater formation timescale of $t > 600$ s. This also means that the impact was most likely within the gravity-controlled regime rather than the strength-controlled in agreement with the conclusion of A. F. Cheng et al. (2024).

A related analysis by A. M. Stickle et al. (2025) using complex impact models also examined the relationship between $Y$ and $M$ while attempting to match the $\Delta V$ (reduction in Dimorphos' along-track orbital velocity component) and $\beta$ values calculated by A. F. Cheng et al. (2023). Their initial results suggested values of $Y$ ranging from $\sim$1 Pa to $\sim$10 kPa. After taking into account LICIACube observations and mass estimates from other studies, they are able to constrain to $Y < 500$ Pa. They state that this could be lower still given additional factors such as the geometric simplification of the boulders at the impact site or treating the DART spacecraft as a combination of three spheres.

Further support for a gravity-controlled impact came from the A. F. Cheng et al. (2024) LICIACube image analysis. They state that no evidence for plume detachment was seen, along with a qualitative inference of the inner region being optically thick, which are both factors consistent with a gravity-controlled impact as discussed above. We can confirm, quantitatively, the optically thick nature of the inner plume region (see Figures 9 and 12). Interestingly, our study and theirs reached similar conclusions despite differences in the scattering model used for their optical depth modeling. Our retrieval results invoked a single power law, while they assumed the broken power law seen in HST tail modeling/observations (J.-Y. Li et al. 2023; F. Moreno et al. 2023). We used a series of particle analogs covering different size regimes and included phase dependence, while they assumed isotropic scattering with $Q_{\mathrm{ext}} = 2$ for all particle sizes.

Finally, if we also take into consideration the likely reshaping of Dimorphos seen in the model results of S. D. Raducan et al. (2024) and suggested by lightcurve observations (P. Pravec et al. 2024; P. Scheirich et al. 2024), then it is even more likely that the impact is at the very-low-strength end of the gravity-controlled regime. This occurs since values of $Y < 5$ Pa can result in reshaping of Dimorphos rather than a crater (S. D. Raducan & M. Jutzi 2022; A. F. Cheng et al. 2024; S. D. Raducan et al. 2024).

## 7. Conclusions

Analysis of LICIACube/LUKE camera brightness measurements at widely separated phase angles was used to constrain ejecta mass using the size dependence of the scattering phase function. This was combined with a retrieval to calculate mass estimates for an optically thin plume. Calculating quasi-independent estimates of mass for each RGB channel yielded a lower limit mass estimate range for the optically thin portion of the plume within the LUKE FOV of 0.85 to $1.19 \times 10^7$ kg. This was found to be consistent with mass estimates by others based on HST and ground-based observations (Table 2, Section 6.1).

Using a single wide-field high-SNR image (Image #0, green channel), an empirical extrapolation of areal mass density to the image center yields an estimate of additional mass in the optically thick inner plume region, and a total plume mass of $1.6 \pm 0.3 \times 10^7$ kg, which we regard as a plausible upper limit for mass within the LUKE FOV. Though it is likely that a high-speed population of very small particles left the LICIACube FOV prior to our observations, such a population would represent <1% of our derived plume mass, a value much smaller than our uncertainties. Taking into account a boulder contribution increases our total mass estimate to possible maximum of $2.4 \times 10^7$ kg.

Analysis of a systematic decline in $I/\mathcal{F}$ with phase angle indicates that plume fragments about a millimeter or larger in size dominate the plume scattered light at visible wavelengths, in agreement with other studies.

It was found that the ejecta particle size distribution during the LICIACube imaging period was best represented by a single power law ($k = -2.5$), rather than the broken law seen in later HST-based modeling/observation efforts. This is possibly due to size-sorting processes driven by SRP not having had enough time to have significantly modified the size distribution.

Our ejecta mass estimates are consistent with Dimorphos having weak cohesive strength (strength <5000 Pa based on the optically thin estimate and more likely in the 50 Pa range) when taking the empirical total mass estimate plus boulder contribution, with an impact that was in the gravity-controlled regime. We remark that the LUKE observations were <243 s after impact, so the crater formation process for a gravity-regime impact (>600 s) may not have finished by then; i.e., the mass release process was ongoing.

## Acknowledgments

This research was supported by the NASA/GSFC Internal Scientist Funding Model (ISFM) Exospheres, Ionospheres, Magnetospheres Modeling (EIMM) team, and the NASA Solar System Exploration Research Virtual Institute (SSERVI LEADER: Lunar Environment and Dynamics for Exploration Research). The work done through the Center for Research and Exploration in Space Science and Technology (CRESST-II) is supported by NASA award No. 80GSFC24M0006. We thank the LICIACube team https://www.ssdc.asi.it/liciacube/lcc_team.php. This work was supported by the Italian Space Agency (ASI) in the LICIACube project (ASI-INAF agreement AC No. 2019-31-HH.0 CUP F84I190012600). E.D., E. M.E., V.D.C., P.H.H., J.D.P.D., A.R., A.Z. acknowledge the Italian Space Agency (ASI) for the agreement No. 2019-31-HH.0. E.D., E.M.E., P.H.H., J.D.P.D., A.R. acknowledge ASI for the agreement No. 2022-8-HH.0. Research by OM has been supported by PID2021-123370OB-100/AEI/10.13039/501100011033/FEDER.

## Appendix A
## LUKE Absolute Response

We obtained the LUKE RGB absolute response using the results of Pleiades observations, taken during the LICIACube, approach phase, as listed in the L1+ archive and made available on the DART SOC around 2023 March 30. A debayering process had been incorporated in this archive, along with instrument linearity corrections. Since the Pleiades member stars span an order of magnitude in brightness, they provide a reliable verification of instrument response, as well as a self-consistent check on response linearity. Three Pleiades observations were studied (Table 3), resulting in a data set large enough for meaningful uncertainty estimates. The possible influence on the calibration from nebulosity surrounding the Pleiades was found to be insignificant, by using the $\xi^2$ Ceti measurement. Source files analyzed by us are listed in Table 3.

We derive the factors $S_R$, $S_G$, $S_B$ that relate measured per-pixel signal to band-averaged intensity (W m$^{-2}$ nm$^{-1}$) of an extended source at the LUKE aperture. Given a color dependent, point-spread function (PSF) extending over multiple pixels, $S_{R,G,B}$ can be obtained from a star measurement by

$$S_{R,G,B}\left(\sum{}^{\star}\right)_{R,G,B}\Omega_{px} = \bar{\mathcal{F}}_{R,G,B}, \tag{A1}$$

where $(\sum^{\star})_{R,G,B}$ is the total star signal collected over multiple pixels, $\Omega_{px}$ is the single-pixel solid angle ($6.09 \times 10^{-9}$sr), and $\bar{\mathcal{F}}_{RGB}$ is the star's band-averaged flux (W m$^{-2}$ nm$^{-1}$).

### A.1. Flux Predictions

The Pleiades fluxes $\bar{\mathcal{F}}_{RGB}$ are obtained by first computing their fluxes ($\bar{\mathcal{F}}_{UBVRI}$) in the Johnson-Cousins (JC) UBVRI bands (M. S. Bessell 1990), utilizing listed magnitudes (https://simbad.u-strasbg.fr/simbad/). The zero-point of this system is obtained using a model spectrum of Vega, available from the STScI stellar spectral library (R. C. Bohlin et al. 2020), and integrating this model over the set of normalized UBVRI standard shapes. Adopting standard definitions for the JC system, i.e., $m_{Vega} = 0.03$, with zero magnitude A0V star = 0.0 and all colors = 0.0, the flux from each star $i$ is then computed in each JC band $k$ using the corresponding Vega flux $\bar{\mathcal{F}}_{(0,k)}$,

$$\bar{\mathcal{F}}_{i,k} = \bar{\mathcal{F}}_{0,k}\, 10^{0.4(0.03 - m_{i,k})}. \tag{A2}$$

The set of node wavelengths and fluxes is then used to estimate $\bar{\mathcal{F}}_{RGB}$ by integrating a piecewise linear spectrum of each star over the LUKE bandpass shapes, as in Figure 15. We point out that the UBVRI system encompasses the full spectral range of the LUKE filters (G. Poggiali et al. 2022), which avoids the difficulties of translating RGB measurements to other color systems with wider coverage (W. Park et al. 2016).

To verify consistency with the Pleiades-derived response, we perform a direct integration over the RGB bandpass shapes, using the measured spectrum of spectrophotometric standard star $\xi^2$ Ceti/HR718 (M. Hamuy et al. 1992; available here: http://www.eso.org/sci/observing/tools/standards/spectra). The resulting RGB fluxes are listed in Table 3.

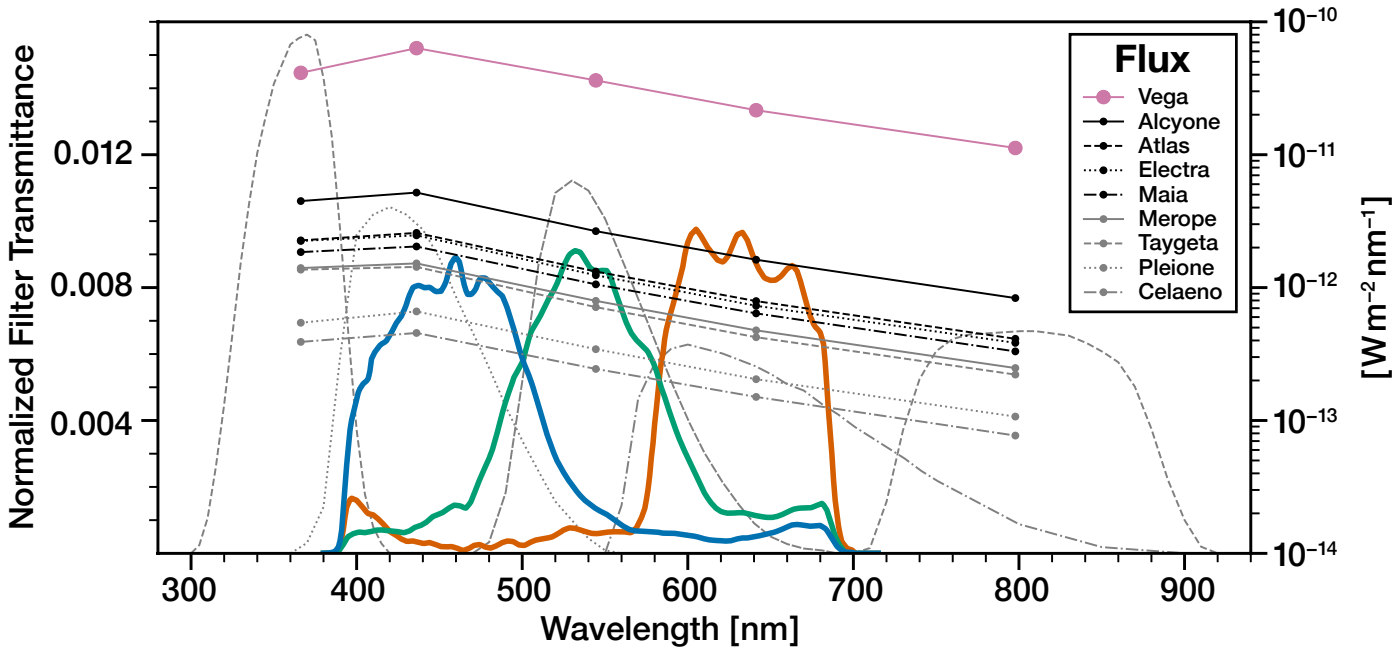


**Figure 15.** Linearly interpolated spectra of the Pleiades, derived from their listed magnitudes (lines with solid circles) used to derive RGB fluxes for calibration. The LICIACube RGB bandpass curves are given by the thick curves colored for each channel, respectively. The dashed lines in the background are for the JC UBVRI bandpass curves.

**Table 3**
Computed Fluxes $\bar{\mathcal{F}}_{\rm RGB}$ in W m$^{-2}$ nm$^{-1}$ for the Pleiades and Standard Star $\xi^2$ Ceti

| Band | Alcyone | Atlas | Electra | Maia | Merope | Taygeta | Pleione | Celaeno | $\xi^2$ Ceti |
|---|---|---|---|---|---|---|---|---|---|
| R | $1.99 \times 10^{-12}$ | $9.80 \times 10^{-13}$ | $9.15 \times 10^{-13}$ | $7.89 \times 10^{-13}$ | $5.90 \times 10^{-13}$ | $5.30 \times 10^{-13}$ | $2.53 \times 10^{-13}$ | $1.83 \times 10^{-13}$ | $5.32 \times 10^{-13}$ |
| G | $2.93 \times 10^{-12}$ | $1.45 \times 10^{-12}$ | $1.37 \times 10^{-12}$ | $1.16 \times 10^{-12}$ | $8.69 \times 10^{-13}$ | $7.92 \times 10^{-13}$ | $3.76 \times 10^{-13}$ | $2.65 \times 10^{-13}$ | $7.74 \times 10^{-13}$ |
| B | $4.20 \times 10^{-12}$ | $2.09 \times 10^{-12}$ | $2.00 \times 10^{-12}$ | $1.66 \times 10^{-12}$ | $1.24 \times 10^{-12}$ | $1.16 \times 10^{-12}$ | $5.35 \times 10^{-13}$ | $3.72 \times 10^{-13}$ | $1.139 \times 10^{-12}$ |

**Table 4**
Source Files for the Stellar Calibration (Available in R. Lolachi et al. 2024)

| Pleiades | $\xi^2$ Ceti |
|---|---|
| Obs. I:liciacube_luke_l2_1663640713_00006_01 | liciacube_luke_l2_1663831839_00000_01 |
| Obs. II:liciacube_luke_l2_1663835259_00000_01 | |
| Obs. III:liciacube_luke_l2_1663835359_00000_01 | |

### *A.2. Measurements*

Table 4 lists the partial filenames of the three Pleiades observations that were used, resulting in a data set large enough for meaningful uncertainty estimates. The three Pleiades observations are listed in chronological order and designated I, II, and III. A single $\xi^2$ Ceti measurement is used for validation.

Figure 16 (left panel) shows a sample, 300 × 300 subframe spanning ≈1.3°, in this example, the Pleiades Obs. I, green channel. For each star, total signal $(\sum^{\star})_{\rm R,G,B}$ is determined by summing all pixel values within an 18-pixel radius ring, after subtracting the average of the surrounding annular region with 3 px width. While Pleione is included in the image, it's measurements are excluded from the analysis due to its proximity to the much brighter Atlas. The 100 × 100 frame (right) shows a 1 s observation of $\xi^2$ Ceti using the same, 18 px radius capture circle. It was located in LICIACube images by comparing observed star positions with starfield images in the SIMBAD object database. While a total of 14, $\xi^2$ Ceti observations were made, low noise at shorter integration times was found to be detrimental, and larger integration times (2 s) exhibited variability possibly related to drift of the stars position between Bayer filter elements (though we did not study this closely). Only two, 1 s observations were optimal, and only one (the Table 3 observation) was chosen.

Row and column profiles through Alcyone (not included here) show the RGB shapes of the LUKE PSF. A broad, low-level pedestal is apparent in the blue channel, which has been attributed by one of us (Della Corte) to chromatic aberration. Curves showing the cumulative growth in signal with ring radius suggest that the blue signal may be underrepresented by as much as 10%, which would lead to brightness and plume mass overestimates. This was difficult to ascertain since, beyond ≈18 px ring radius, uncertainty rapidly increases due

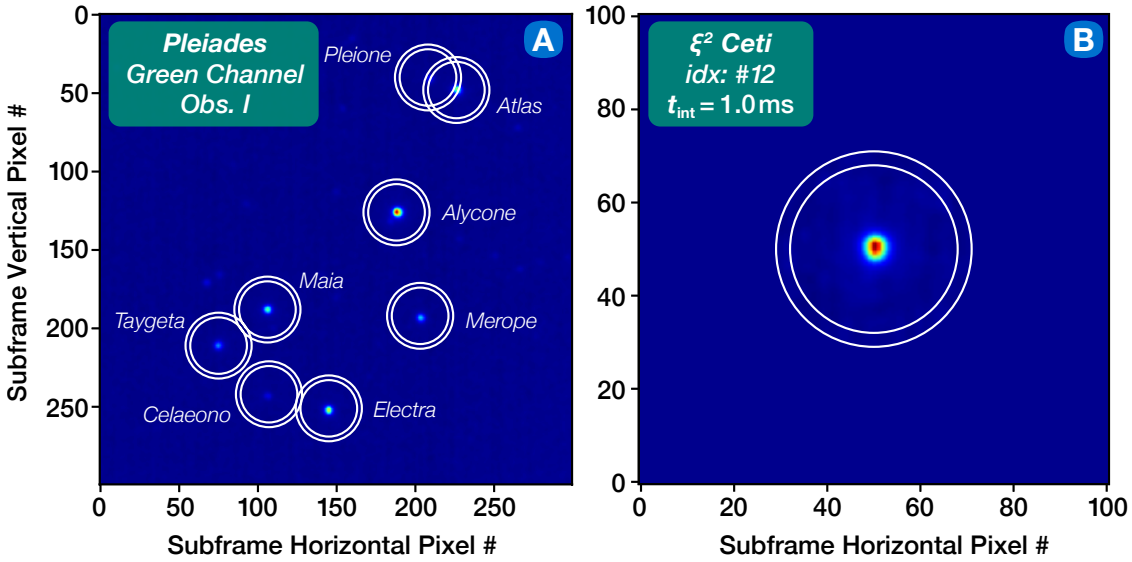


**Figure 16.** Sample LUKE observations of the (A) Pleiades and (B) $\xi^2$ Ceti (see the text). Pixel signals within an 18 pixel radius are summed. Bias and background corrections are made by subtracting the mean of the annular points from the interior values. Pleione is excluded from this analysis because of its proximity to the much brighter Atlas.

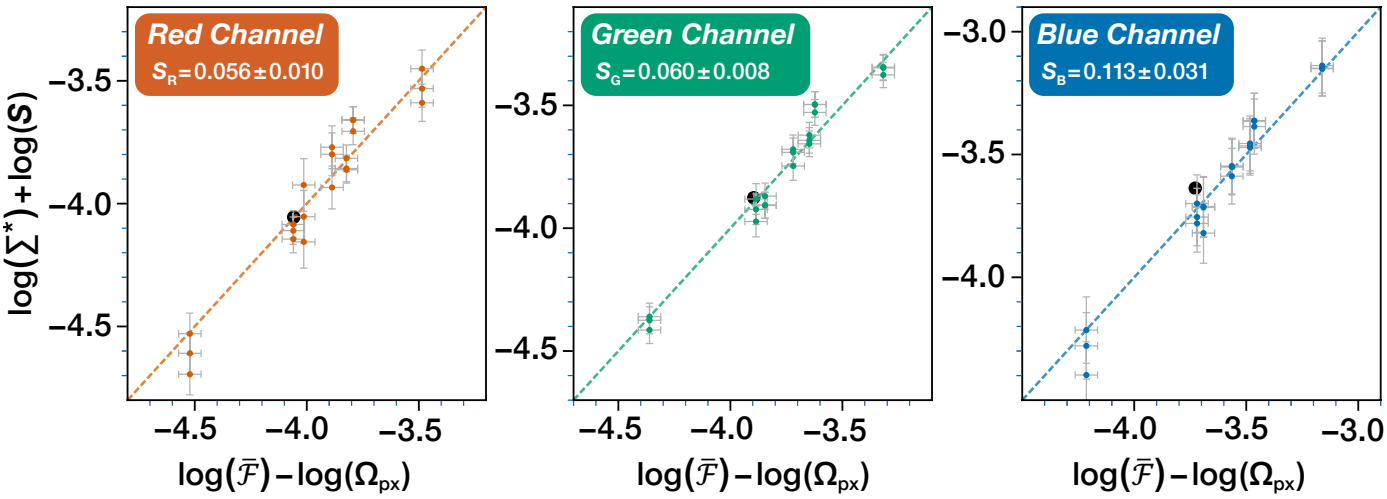


**Figure 17.** Scatter plot showing Pleiades-derived conversion factors $S_R$, $S_G$, $S_B$ and their uncertainties. Applying these conversions to measurements of standard star $\xi^2$ Ceti (filled, black circles) demonstrates overall consistency of the calibration.

to background variability, overlap, and possible contributions from weak field stars.

### *A.3. Estimating LUKE Conversion Factors* $S_R$, $S_G$, $S_B$

To obtain $S$ in each band, one can now create a plot of $S_{R,G,B}(\sum^{\star})_{R,G,B}$ against $\bar{\mathcal{F}}_{R,G,B}/\Omega_{px}$, and find the best-fit values of $S$ (slope) through the Pleiades measurements. It is observed that variability in pixel signal is proportional to the signal values themselves, suggesting that measurement scatter is related to small drifts in instrument responsivity over time, more so than Poisson noise (Obs. I and Obs. III were separated by some 54 hr. If the log of these quantities is plotted instead, then a single value of uncertainty is used to label the $\log(\sum^{\star})$ values, and $\log(S_{R,G,B})$ becomes an additive constant, and as illustrated in Figure 17. For each band, we define

$$xpts_{3i} = \log \bar{\mathcal{F}}_{3i} - \log \Omega_{px} \tag{A3}$$

and

$$ypts_i = \log S + \log\left(\sum^{\star}\right)_i, \tag{A4}$$

Here, "3$i$" is a shorthand notation indicating that each of the $i = 1$ to 7 predicted Pleiades fluxes is repeated three times, in order to pair with results from three observations. $\log S$ is then determined by an unweighted $\chi^2$ minimization,

$$\frac{\partial \sum_i^{21} (xpts_{3i} - ypts_i)^2}{\partial \log S} = 0, \tag{A5}$$

leading to a simple linear solution,

$$\log S = \langle log\ \bar{\mathcal{F}} \rangle - \left\langle \log \sum^{\star} \right\rangle - \log \Omega_{px}. \tag{A6}$$

### A.4. S Uncertainties

We define an $x$-variance $\sigma_x^2 = (0.4\Delta m)^2$ assuming a fixed magnitude error $\Delta m \approx 0.05$ in the SIMBAD database. The $y$-variance is set by the same quantity, plus scatter in the measurements, the latter dominating the $y$-uncertainty.

$$\sigma_y^2 = \sigma_x^2 + \frac{1}{24}\sum_k (xpts_{3i} - ypts_k)^2. \tag{A7}$$

Then the total uncertainty $\sigma_{\log S}$ is

$$\sigma_{\log S} = \sqrt{\left(\frac{\partial \log S}{\partial(\log \bar{\mathcal{F}})}\right)^2 \sigma_x^2 + \left(\frac{\partial \log S}{\partial\left(\log\sum^{\star}\right)}\right)^2 \sigma_y^2} \tag{A8}$$

$$= \sqrt{\sigma_x^2 + \sigma_y^2}, \tag{A9}$$

where we recognize that

$$\left(\frac{\partial \log S}{\partial(\log \bar{\mathcal{F}})}\right)^2 = \left(\frac{\partial \log S}{\partial\left(\log\sum^{\star}\right)}\right)^2 = 1. \tag{A10}$$

Giving us the formal expression for $\sigma_S$,

$$\sigma_S = \frac{dS}{d\log S}\,\sigma_{\log S} = S \ln 10\, \sigma_{\log S}. \tag{A11}$$

## Appendix B
## Plume Mass–Brightness Relations

One can relate total plume mass in the LUKE FOV to plume radiant intensity (total brightness) in each band, since both depend on the overall concentration of particles and their size distribution. Except for the innermost region of the plume (within a few tens of meters from Dimorphos), we consider the plume to be optically thin, i.e., geometric optical depth less than ≈0.2 as verified by comparisons with multiple-scattering simulations (R. Lolachi et al. 2023a). Under these conditions, mass and brightness along each line of sight (LOS) are proportional, leading to straightforward relations between these quantities.

Here we allow for the possibility of a broken power-law size distribution $dN/da \sim a^{k_i}$ with $k_1 \approx -2.6$ and $k_2 = -3.5$ to 3.7, as discussed by J.-Y. Li et al. (2023) and F. Moreno et al. (2023), from an analysis of HST and ground-based measurements of the evolving tail. Coefficient $k_1$ defines the distribution from $a_{\rm min}$ to a transition grain radius $a_{\rm t}$, and $k_2$ from $a_{\rm t}$ to a maximum radius $a_{\rm max}$, with nominal values of 1 $\mu$m, 3 mm, and 5 cm for $a_{\rm min}$, $a_{\rm t}$ and $a_{\rm max}$. Defining $N$ as particle concentration, the differential particle abundance in the two size segments is

$$\frac{dN}{da} = {\rm c}_{1,2}\, a^{k_{1,2}}, \tag{B12}$$

where ${\rm c}_{1,2}$ are coefficients that can be treated as weighting factors. Differential mass is likewise

$$\frac{dM}{da} = \frac{4\pi\rho}{3}\, a^3 \left(\frac{dN}{da}\right)_{1,2}, \tag{B13}$$

with $\rho$ being the particle mass density, taken to be 3500 kg m$^{-3}$ (Section 4). Integrating to obtain the total mass

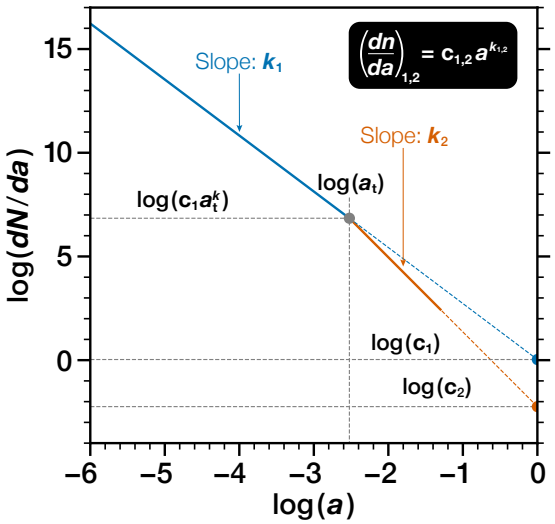


**Figure 18.** Graphical representation of the broken power-law size distribution for distinctly different $k$-values ($k_1 = -2.7$ and $k_2 = -3.6$).

is straightforward, resulting in

$$M = \frac{4\pi\rho}{3}\left[{\rm c}_1 \cdot \frac{a_{\rm t}^{k_1+4} - a_{\rm min}^{k_1+4}}{k_1+4} + {\rm c}_2 \cdot \frac{a_{\rm max}^{k_2+4} - a_{\rm t}^{k_2+4}}{k_2+4}\right]. \tag{B14}$$

The ratio ${\rm c}_1/{\rm c}_2$ can be easily recognized with the help of a log–log plot showing the particle size distribution parameters (Figure 18). Though the equation is undefined when $k = -4$, the range of valid values of $|k|$ lies well below this magnitude (see Figure 10). At the intercept,

$$\log({\rm c}_1) = \log({\rm c}_1\, a_{\rm t}^{k}) - k_1 \log(a_{\rm t}) \tag{B15}$$

$$\log({\rm c}_2) = \log({\rm c}_1\, a_{\rm t}^{k}) - k_2 \log(a_{\rm t}). \tag{B16}$$

Subtracting these equations leads to

$$\frac{{\rm c}_1}{{\rm c}_2} = a_{\rm t}^{k_2-k_1}. \tag{B17}$$

Equation (B14) therefore contains only a single unknown scale factor ${\rm c}_1$ (note that ${\rm c}_2$ could have been substituted instead),

$$M = \frac{4\pi\rho}{3}\, {\rm c}_1\, S_M, \tag{B18}$$

with the mass factor $S_M$ defined as

$$S_M(a_j, k_i) = \left(\frac{a_{\rm t}^{k_1+4} - a_{\rm min}^{k_1+4}}{k_1+4}\right) + a_{\rm t}^{k_1-k_2}\left(\frac{a_{\rm max}^{k_2+4} - a_{\rm t}^{k_2+4}}{k_2+4}\right), \tag{B19}$$

noting that $a_{\rm t}^{(k_1-k_2)} = {\rm c}_2/{\rm c}_1$. The dependencies $a_j$, $k_i$ are compact representations for $a_{\rm min}$, $a_{\rm t}$, $a_{\rm max}$, and $k_1$, $k_2$, respectively.

### B.1. Mass–Brightness Relation

Defining $I(\alpha)$ as plume radiant intensity (W sr$^{-1}$ nm$^{-1}$), then differential intensity $dI(\alpha)/da$ and particle concentration

$dN/da$ are once again divided in the two size segments,

$$\frac{dI(\alpha)}{da} = \frac{\bar{J}_\odot}{\pi} A_p(a, \alpha)\, \pi a^2 \left(\frac{dN}{da}\right)_{1,2}, \tag{B20}$$

with $\bar{J}_\odot$ being the band-average solar flux (Section 3) determined separately over each of the LUKE filter response functions, and computed to be $\bar{J}_{\odot R}$=1.65, $\bar{J}_{\odot G}$=1.86 and $\bar{J}_{\odot B} = 1.87\ \mathrm{W m^{-2}\, nm^{-1}}$. The factor $A_p(a, \alpha)$ is the particle physical albedo at phase angle $\alpha$ (Section 3). Equation (B20) is then integrated in a similar way

$$I_{\mathrm{mdl}}(\alpha, a_j, k_i) = \bar{J}_\odot\, \mathrm{c}_1\, S_I(\alpha, a_j, k_i) \tag{B21}$$

with intensity factor,

$$S_I(\alpha, a_j, k_i) = \int_{a_{\min}}^{a_t} A_p(a, \alpha)\, a^{k_1+2} da + a_t^{k_1-k_2} \int_{a_t}^{a_{\max}} A_p(a, \alpha)\, a^{k_2+2} da, \tag{B22}$$

Subscript "mdl" designates "model," to distinguish it from the measured intensities.

The factor $\mathrm{c}_1$ can then be eliminated in Equations (B18) and (B21) to form a plume mass–radiance relation for each of the RGB bands

$$I_{\mathrm{mdl}}(\alpha, a_j, k_i) = \frac{\bar{J}_\odot}{\pi} \frac{3}{4\rho} \frac{S_I(\alpha, a_j, k_i)}{S_M(a_j, k_i)} M. \tag{B23}$$

In the case where LICIACube results show no evidence of a broken power law (i.e., $k_1 \approx k_2$), then $\mathrm{c}_1 = \mathrm{c}_2$, the scale factor $a_t^{(k_1-k_2)}$ becomes 1.0 and segments 1, 2 of both $S_M$ and $S_I$ will have equal weight.

## Appendix C
## Millimeter Grain Geometric Albedo Curve, from Bennu Particle Photometry

Particles in the millimeter-size range represent the important transition region between the forward scattering behavior of small grains (negative phase coefficient), and the phase functions of large fragments, e.g., rocks and boulders, that monotonically decline in brightness with increasing phase angle. Photometric (though spatially unresolved) measurements of naturally ejected, millimeter-sized particles from Bennu were made over narrow phase-angle windows using the OSIRIS-REx navigation cameras, as described by C. W. Hergenrother et al. (2020). Supplementary details of these measurements are available from S. R. Chesley et al. (2020a, 2020b).

We have found that values of phase coefficients ($dm/d\alpha$) measured for the Bennu particles were spread more-or-less evenly between that of two laboratory-measured "pebbles" by O. Muñoz et al. (2017, 2020) at similar phase angles; in particular, a dark, porous volcanic sample (Etna) and a more compact, and visibly higher albedo pyroxene glass (MgFeAlSi) sample (C. Jaeger et al. 1994), with spherical volume-equivalent radii of ≈3.5 and 2.8 mm, respectively. This allowed a representative millimeter-grain albedo curve to be computed for each Bennu particle in several steps: relative magnitude curves were computed for the two laboratory samples particles. The resulting phase coefficient curves are used as basis functions, from which interpolated phase functions for the Bennu particles could be obtained. Using the results of Bennu absolute photometry, we convert these phase functions to geometric albedo curves $A_p(\alpha)$, taking into account the very different albedos of the parent bodies (Bennu versus Didymos). These curves are then averaged to represent the millimeter-Grains category in Section 3, along with the uncertainty in this profile.

### C.1. Reference (Basis) Phase-coefficient Curves $\beta_H$, $\beta_L$

Figure 19 (left-hand side) shows the laboratory phase function measurements (symbols), scaled to 1.0 at $\alpha = 150°$. Smoothed phase curves are created by interpolating along the measurements at 1° spacing. The curves are extended to 0° at constant phase coefficient, by fitting to several of the small phase measurements. In the case of MgFeAlSi, the first few measurements show an abrupt upturn that is likely to be a measurement artifact and not related to opposition brightening. From a survey of millimeter-sized scattering measurements available in the Granada–Amsterdam scattering database (https://scattering.iaa.es/), no other sample shows a similar upturn. Consequently, we reject the first five measurement points, shown faded in the plot.

The right-hand side (dashed lines) shows the corresponding relative magnitude curves, expressed as difference curves $\Delta m$ ($\alpha$), where $\Delta m = m - m(\alpha = 0°)$,

$$\Delta m(\alpha) = -2.5 \log\left(\frac{F_{11}(\alpha)}{F_{11}(\alpha = 0°)}\right). \tag{C24}$$

These $\Delta m$ curves, which exhibit very different slopes, were differentiated, resulting in reference (i.e., basis) functions, $\beta_{\mathrm{H}}$, $\beta_{\mathrm{L}}$ (for MgFeAlSi and Etna, respectively) and used to create interpolated phase coefficient curves $\beta_p(\alpha)$, for each of the Bennu particles.

$$\beta_{\mathrm{H,L}} = -\frac{dm}{d\alpha}\ [\mathrm{mag}/^\circ] \tag{C25}$$

This differencing step greatly amplifies measurement noise, as shown in Figure 20. Smoothed versions of these shapes are therefore created using cubic spline functions, with knot locations chosen subjectively ("walked in") for best visible agreement. (This step was done iteratively by comparing reconstructed versions of $\Delta m$ with the measurements.)

### C.2. Particle Phase-coefficient Curves ($\beta_{\mathrm{j}}$)

Table 5, taken from C. W. Hergenrother et al. (2020) and S. R. Chesley et al. (2020b, 2020a), lists the Bennu particle measurements and derived spherical volume-equivalent radii. In Table 5, $H$ and $V_{11}$ follow customary definitions, namely that $H$ is the particle's apparent ($V$-band) magnitude at zero phase and 1 au from the Sun. Reduced magnitude $V_{11}$ has a similar definition, except it is defined at the observed phase angle. While values of $V_{11}$ are not explicitly stated by the authors, we have translated $H$ back to $V_{11}$ using their method of extrapolating measurements to zero-phase using the average phase coefficient of the collection (0.013 mag/°).

Measured particle phase coefficients are indicated in Figure 21 at the center of the observed phase-angle windows (gray dots). Designating $\beta_j(\bar{\alpha}_j)$ as the measured phase coefficient of particle $j$, at mean phase angle $\bar{\alpha}_j$, we can then, for each particle, compute an interpolation parameter $f_j$, giving

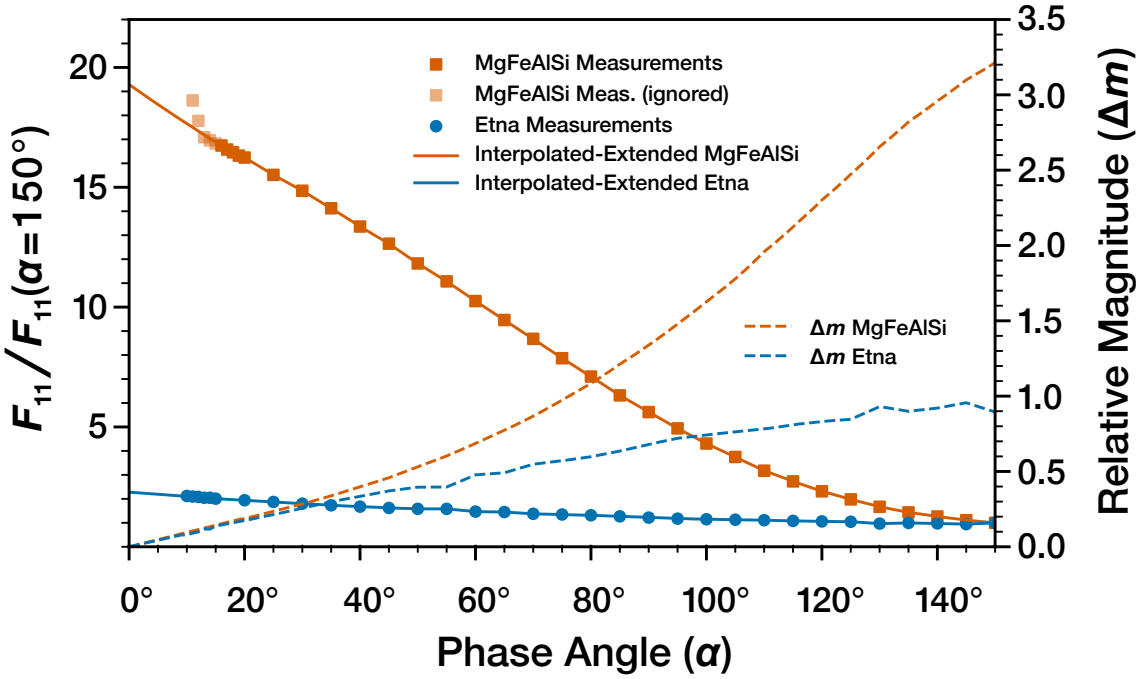


**Figure 19.** Phase functions ($F_{11}$) of millimeter-grains with very different brightness slopes (left-hand side). Relative magnitude curves ($\Delta m$) are shown as dashed lines.

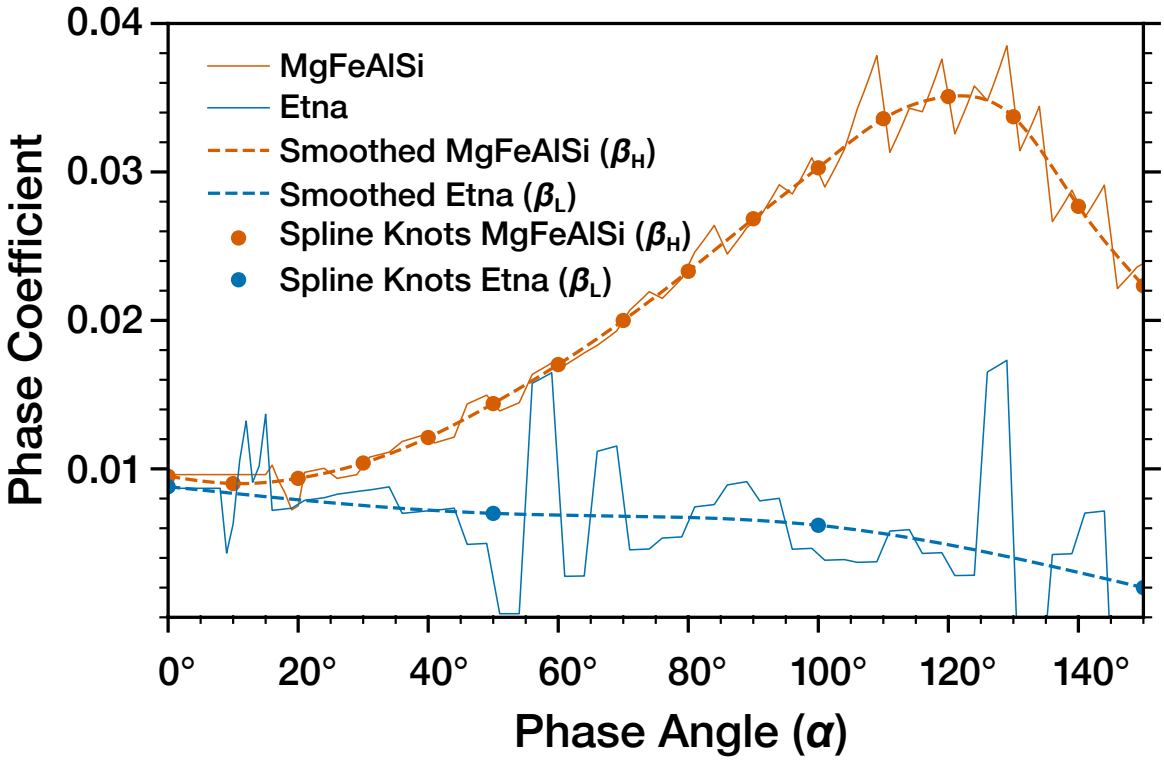


**Figure 20.** Curves showing phase coefficient ($-dm/d\alpha$) obtained from Figure 19. Smoothed versions of these curves (dashed lines) form the basis functions for creating interpolated phase coefficient curves of the Bennu particles.

the fractional distance between the basis-function values at $\bar{\alpha}_j$,

$$f_j = -\frac{\beta_j(\bar{\alpha}_j) - \beta_{\rm L}(\bar{\alpha}_j)}{\beta_{\rm H}(\bar{\alpha}_j) - \beta_{\rm L}(\bar{\alpha}_j)}. \quad \text{(C26)}$$

These values of $f_j$ are then used to create the set of interpolated particle phase coefficient curves,

$$\beta_j(\alpha) = f_j\,\beta_{\rm H}(\alpha) + (1 - f_j)\beta_{\rm L}(\alpha), \quad \text{(C27)}$$

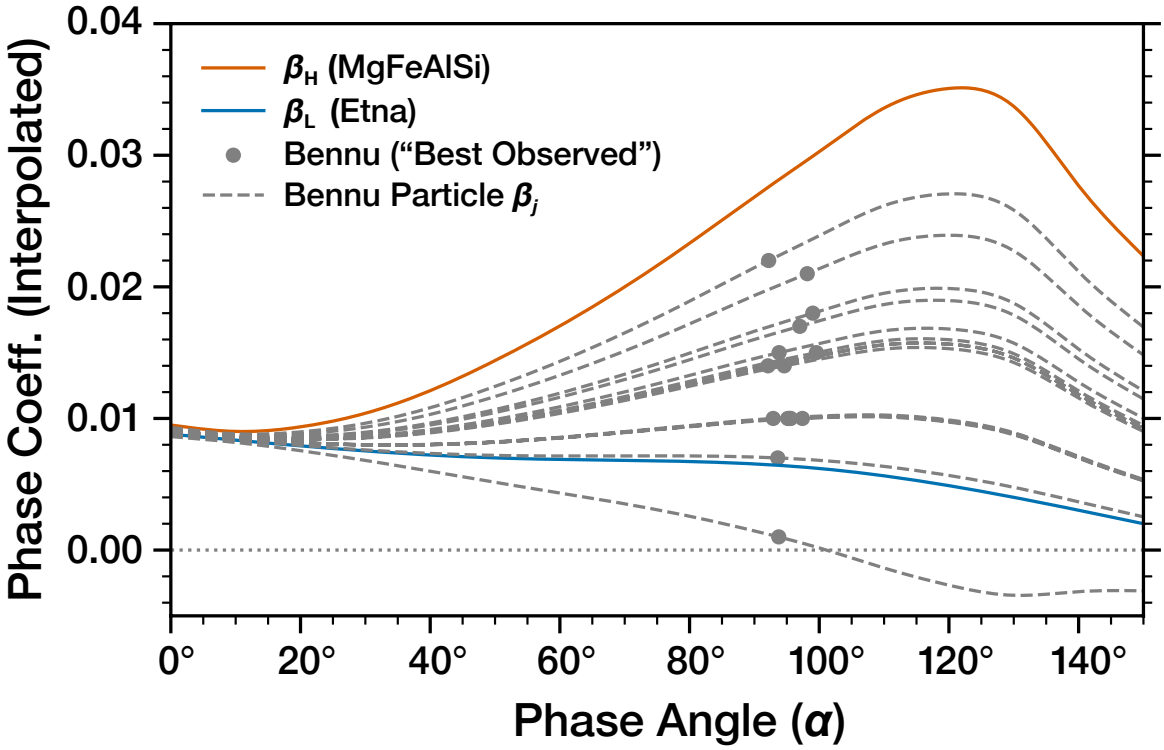


**Figure 21.** Interpolated phase coefficient curves for Bennu particles, obtained from locations of phase coefficients of "Best Observed" particles (C. W. Hergenrother et al. 2020) and their fractional distance between basis functions $\beta_H$ and $\beta_L$.

**Table 5**
"Best Observed" Particles from C. W. Hergenrother et al. (2020) and $a_{VE}$

| Particle Desig. | Phase Angle ($\alpha$) (°) ($\alpha_{min}$ – $\alpha_{max}$, $\bar{\alpha}$) | Phase Coeff. $dm/d\alpha$ | Abs. Mag $H$ | Red. Mag $V_{11}(\bar{\alpha})$ | $a_{VE}$ (mm) | $f_p$ |
|---|---|---|---|---|---|---|
| P1 | 73.9–110.3, 92.1 | 0.014 (0.001) | 42.84 (0.13) | 44.04 | 8.3 | 0.356 |
| P2 | 77.3–107.1, 92.2 | 0.022 (0.002) | 41.58 (0.14) | 42.78 | 13.3 | 0.735 |
| P3 | 81.1–110.1, 95.6 | 0.010 (0.002) | 42.90 (0.25) | 44.14 | 7.5 | 0.162 |
| P15 | 80.5–117.5, 99.0 | 0.018 (0.002) | 44.85 (0.21) | 46.14 | 2.8 | 0.496 |
| P16 | 80.5–110.4, 95.5 | 0.010 (0.001) | 44.57 (0.14) | 45.81 | 3.6 | 0.162 |
| P41 | 74.9–110.9, 92.9 | 0.010 (0.002) | 42.68 (0.20) | 43.89 | 10.7 | 0.165 |
| P213 | 77.3–113.0, 95.2 | 0.010 (0.003) | 44.39 (0.25) | 45.63 | 3.8 | 0.162 |
| P247 | 78.9–108.3, 93.6 | 0.007 (0.001) | 42.91 (0.10) | 44.13 | 6.6 | 0.257 |
| P251 | 79.0–108.6, 93.8 | 0.015 (0.001) | 44.18 (0.06) | 45.40 | 3.8 | 0.394 |
| P266 | 87.0–112.1, 99.6 | 0.015 (0.004) | 44.67 (0.45) | 45.96 | 3.1 | 0.367 |
| P269 | 86.2–107.8, 97.0 | 0.017 (0.003) | 43.38 (0.28) | 44.64 | 6.0 | 0.466 |
| P273 | 80.5–114.3, 97.4 | 0.010 (0.003) | 44.79 (0.27) | 46.06 | 2.9 | 0.160 |
| P289 | 82.3–114.0, 98.2 | 0.021 (0.002) | 43.74 (0.22) | 45.02 | 4.5 | 0.630 |
| P303 | 81.2–106.3, 93.8 | 0.001 (0.002) | 45.29 (0.21) | 46.51 | 2.8 | −0.251 |
| P369 | 83.6–105.6, 94.6 | 0.014 (0.008) | 45.03 (0.81) | 46.26 | 2.5 | 0.345 |

**Note.** "Best Observed" particles from C. W. Hergenrother et al. (2020), and derived spherical volume-equivalent radii, $a_{VE}$, obtained from S. R. Chesley et al. (2020a, 2020b). The last column is the basis-function interpolation parameter described below.

shown as gray dashed lines shown in Figure 21. One particle (P303) shows a measured coefficient that is smaller than $\beta_L$ and becomes <0. Such a curve leads to a modest increase in brightness at large phase angles. This is entirely physically plausible, since millimeter-grains lie in the size transition region between small grains and larger fragments. Given the size range of Bennu particles, one might anticipate an observable correlation between phase coefficient and particle size. However, a simple comparison plot (not included) of values in Table 5, did not reveal any such relation.

### C.3. Particle Phase Functions and Geometric Albedos

Using the derived phase coefficients, it was possible to construct relative magnitude curves for each particle as a series of partial sums, as shown in Figure 22(A). Defining $i$ as the 1° phase-angle index, then for each particle $j$,

$$\Delta m_{i,j} = \sum_{i=1}^{i_{max}} [\Delta m_{i-1,j} + \beta_j \Delta\alpha] \quad \text{(C28)}$$

with $\Delta m(0, j) = 0$, $\Delta\alpha_i = \Delta\alpha = 1°$, and $i_{max} = 150$. Along with the particle $\Delta m$ curves, we also verified the end-to-end

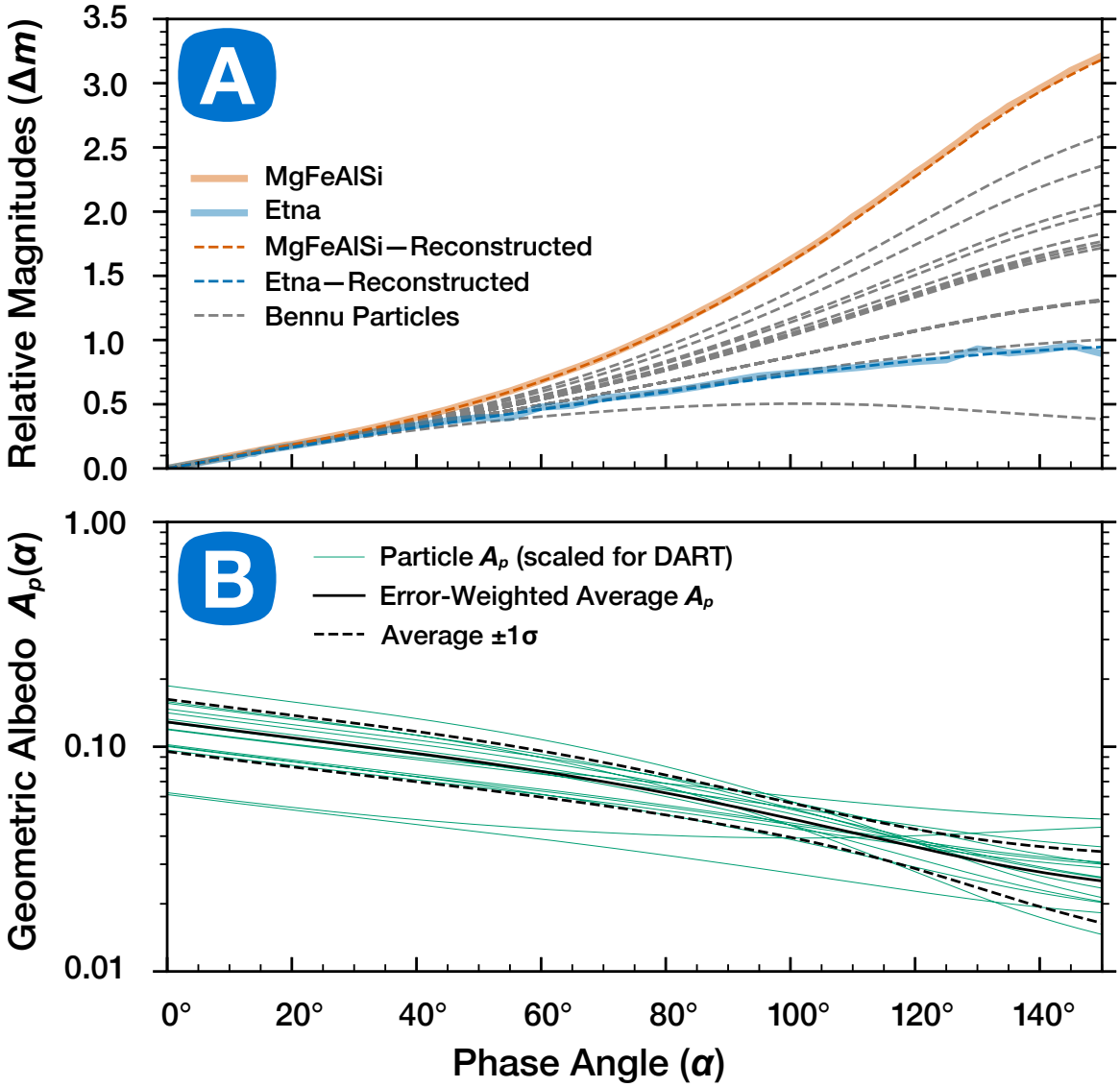


**Figure 22.** Panel (A): interpolated phase coefficient curves for Bennu particles, obtained from the phase coefficients and positions of "Best Observed" particles (C. W. Hergenrother et al. 2020) and their fractional distance between basis functions $\beta_H$ and $\beta_L$. Panel (B): resulting plots of physical albedo (green lines) after correcting for Didymos/Bennu albedo ratio. The black line shows the error-weighted average, and dashed lines represent $1\sigma$ uncertainties.

accuracy of this approach by reconstructing the relative magnitudes of the references themselves using their smoothed basis functions (red and blue dashed curves).

Again, designating the particles by index $j$, $A_p$ curves are created and scaled to the DART environment by first computing revised values for absolute magnitude, $H_j$. These are obtained by translating Bennu $V_{11}(\bar{\alpha}_j)$ to zero phase using the relative magnitude curves,

$$H_j = V_{11,j} - \Delta m_j(\bar{\alpha}_j) - 2.5\log\left(\frac{0.12}{0.044}\right). \tag{C29}$$

The last term in Equation (C29) is a correction for the albedos of the parent bodies. A value of 0.12 (in lieu of ≈0.16) is used for Didymos since, as commented above, the laboratory measurements of particles in this size range exhibit little or no opposition brightening. Zero-phase geometric albedos $A_{p0}$ are then computed using the relation between $A_{p0}$, particle volume-equivalent diameter $D_{VE}$, and absolute magnitude (P. Pravec & A. W. Harris 2007; C. W. Hergenrother et al. 2020). One gets

$$A_{p0,j} = \frac{1.77 \times 10^{16}}{D_{\mathrm{V\,E},j}^2} \cdot 10^{-0.4H_j} \tag{C30}$$

with $D_{VE}$ in centimeters. The set of geometric albedo curves (light-green lines in Figure 22(B)) then follows from Equation (C30) and the relative magnitude curves,

$$A_{p,j}(\alpha) = A_{p0,j} \cdot 10^{-0.4\Delta m_j(\alpha)}. \tag{C31}$$

The average curve, shown as a heavy black line, is a weighted average of the component curves, weighted as the reciprocal of fractional errors in the phase coefficients listed in Table 5. Dotted lines show the $1\sigma$ departure from the average curve. This curve and $\pm 1\sigma$ results represent the average and upper/lower limits for millimeter-grains in the collection of $A_p$ curves.

## ORCID iDs

Ramin Lolachi https://orcid.org/0000-0001-5764-7639
David A. Glenar https://orcid.org/0000-0003-2155-3854
Timothy J. Stubbs https://orcid.org/0000-0002-5524-645X
Ludmilla Kolokolova https://orcid.org/0000-0002-9321-3202
Olga Muñoz https://orcid.org/0000-0002-5138-3932
Tony L. Farnham https://orcid.org/0000-0002-4767-9861
Masatoshi Hirabayashi https://orcid.org/0000-0002-1821-5689
Pedro H. Hasselmann https://orcid.org/0000-0003-1193-8945
Vincenzo Della Corte https://orcid.org/0000-0001-6461-5803
J. D. Prasanna Deshapriya https://orcid.org/0000-0002-5758-1286
Elisabetta Dotto https://orcid.org/0000-0002-9335-1656
Elena Mazzotta Epifani https://orcid.org/0000-0003-1412-0946
Alessandro Rossi https://orcid.org/0000-0001-9311-2869
Angelo Zinzi https://orcid.org/0000-0001-5263-5348

## References

Berezhnoy, A. A., Velikodsky, Y. I., Zubko, E., et al. 2019, P&SS, 177, 104689
Bessell, M. S. 1990, PASP, 102, 1181
Bohlin, R. C., Gordon, K. D., & Tremblay, P. E. 2014, PASP, 126, 711
Bohlin, R. C., Hubeny, I., & Rauch, T. 2020, AJ, 160, 21
Carrier, W. D. I., Olhoeft, G. R., & Mendell, W. 1991, Physical Properties of the Lunar Surface, in Lunar Sourcebook, ed. G. H. Heiken, D. T. Vaniman, & B. M. French (Cambridge: Cambridge Univ. Press), 481
Chabot, N. L., Rivkin, A. S., Cheng, A. F., et al. 2024, PSJ, 5, 49
Chandrasekhar, S. 1960, Radiative Transfer (New York: Dover)
Cheng, A. F., Agrusa, H. F., Barbee, B. W., et al. 2023, Natur, 616, 457
Cheng, A. F., Raducan, S. D., Jutzi, M., et al. 2024, PSJ, 5, 118
Cheng, A. F., Raducan, S. D., Fahnestock, E. G., et al. 2022, PSJ, 3, 131
Cheng, A. F., Stickle, A. M., Fahnestock, E. G., et al. 2020, Icar, 352, 113989
Chesley, S. R., French, A. S., Davis, A. B., et al. 2020a, JGRE, 125, e06363
Chesley, S. R., Hergenrother, C. W., Adam, C., et al. 2020b, Supplementary Data for Bennu Particle Analysis, figshare, doi:10.6084/m9.figshare.11328398.v2
Daly, R. T., Ernst, C. M., Barnouin, O. S., et al. 2023, Natur, 616, 443
de León, J., Licandro, J., Duffard, R., & Serra-Ricart, M. 2006, AdSpR, 37, 178
Deshapriya, J. D. P., Hasselmann, P. H., Gai, I., et al. 2023, PSJ, 4, 231
Dotto, E., Della Corte, V., Amoroso, M., et al. 2021, P&SS, 199, 105185
Dotto, E., Deshapriya, J. D. P., Gai, I., et al. 2024, Natur, 627, 505
Draine, B. T., & Flatau, P. J. 1994, JOSAA, 11, 1491
Dunn, T. L., Burbine, T. H., Bottke, W. F., & Clark, J. P. 2013, Icar, 222, 273
Escobar-Cerezo, J., Palmer, C., Muñoz, O., et al. 2017, ApJ, 838, 74
Farnham, T. L., Hirabayashi, M., Sunshine, J. M., et al. 2025, PSJ, 6, 155
Ferrari, F., Panicucci, P., Merisio, G., et al. 2025, NatCo, 16, 1601
Fitzsimmons, A., Berthier, J., Denneau, L., et al. 2023, LPICo, 2851, 2452
Frattin, E., Muñoz, O., Moreno, F., et al. 2019, MNRAS, 484, 2198
Frattin, E., Martikainen, J., Muñoz, O., et al. 2022, MNRAS, 517, 5463
Gray, Z., Bagnulo, S., Granvik, M., et al. 2024, PSJ, 5, 18
Graykowski, A., Lambert, R. A., Marchis, F., et al. 2023, Natur, 616, 461
Hamuy, M., Walker, A. R., Suntzeff, N. B., et al. 1992, PASP, 104, 533
Hanner, M. S., Giese, R. H., Weiss, K., & Zerull, R. 1981, A&A, 104, 42
Hapke, B. 2012, Theory of Reflectance and Emittance Spectroscopy (2nd edn.; Cambridge: Cambridge Univ. Press)
Hasselmann, P. H., Della Corte, V., Pravec, P., et al. 2024, PSJ, 5, 91
Hergenrother, C. W., Maleszewski, C., Li, J. Y., et al. 2020, JGRE, 125, e06381
Hirabayashi, M., Ferrari, F., Jutzi, M., et al. 2022, PSJ, 3, 140
Hirabayashi, M., Raducan, S. D., Sunshine, J. M., et al. 2025, NatCo, 16, 1602
Housen, K. R., & Holsapple, K. A. 2011, Icar, 211, 856
Hovenier, J. W., & Guirado, D. 2014, JQSRT, 133, 596
Ieva, S., Mazzotta Epifani, E., Perna, D., et al. 2022, PSJ, 3, 183
Jaeger, C., Mutschke, H., Begemann, B., Dorschner, J., & Henning, T. 1994, A&A, 292, 641
Jewitt, D., Kim, Y., Li, J., & Mutchler, M. 2023, ApJL, 952, L12
Kareta, T., Thomas, C., Li, J.-Y., et al. 2023, ApJL, 959, L12
Kim, Y., & Jewitt, D. 2023, ApJL, 956, L26
Lauretta, D. S., Connolly, H. C., Aebersold, J. E., et al. 2024, MAPS, 59, 2453
Li, J.-Y., Hirabayashi, M., Farnham, T. L., et al. 2023, Natur, 616, 452
Lin, Z.-Y., Vincent, J.-B., & Ip, W.-H. 2023, A&A, 676, A116
Lister, T., Constantinescu, C., Ryan, W., et al. 2024, PSJ, 5, 127
Liu, L., Mishchenko, M. I., Hovenier, J. W., Volten, H., & Muñoz, O. 2003, JQSRT, 79, 911
Lolachi, R., Glenar, D. A., & Stubbs, T. J. 2023a, P&SS, 234, 105709
Lolachi, R., Glenar, D. A., Stubbs, T. J., & Kolokolova, L. 2023b, PSJ, 4, 24
Lolachi, R., Glenar, D. A., Stubbs, T. J., et al. 2024, LICIACube LUKE Early DART Investigation Team Release (around 2024-03-30) Plume Images and Stellar Calibration Image Data, v1.0, Zenodo, doi:10.5281/zenodo.14509702
Lolachi, R., Glenar, D. A., Stubbs, T. J., et al. 2025, LPSC 2025, LPI Contributions
Michel, P., Küppers, M., Bagatin, A. C., et al. 2022, PSJ, 3, 160
Moreno, F., Bagatin, A. C., Tancredi, G., et al. 2023, PSJ, 4, 138
Muñoz, O., Frattin, E., Martikainen, J., et al. 2025, JQSRT, 331, 109252
Muñoz, O., Moreno, F., Gómez-Martìn, J. C., et al. 2020, ApJS, 247, 19
Muñoz, O., Moreno, F., Vargas-Martìn, F., et al. 2017, ApJ, 846, 85
Muñoz, O., Volten, H., de Haan, J. F., Vassen, W., & Hovenier, J. W. 2000, A&A, 360, 777
Muñoz, O., Volten, H., Hovenier, J. W., et al. 2007, JGRD, 112, D13215
Muinonen, K., Belskaya, I. N., Cellino, A., et al. 2010, Icar, 209, 542
Muinonen, K., Nousiainen, T., Lindqvist, H., Muñoz, O., & Videen, G. 2009, JQSRT, 110, 1628
Murphy, B. P., Opitom, C., Snodgrass, C., et al. 2023, PSJ, 4, 238
Naidu, S. P., Chesley, S. R., Moskovitz, N., et al. 2024, PSJ, 5, 74
Nousiainen, T., Muñoz, O., Lindqvist, H., Mauno, P., & Videen, G. 2011, JQSRT, 112, 420
Opitom, C., Murphy, B., Snodgrass, C., et al. 2023, A&A, 671, L11
Park, J. S., Liu, Y., Kihm, K. D., & Taylor, L. A. 2006, in 37th Annual Lunar and Planetary Science Conf., ed. S. Mackwell & E. Stansbery (Greenbelt, MD: NASA), 2193
Park, W., Pak, S., Shim, H., et al. 2016, AdSpR, 57, 509
Penttilä, A., Muinonen, K., Granvik, M., et al. 2024, PSJ, 5, 27
Poggiali, G., Brucato, J. R., Hasselmann, P. H., et al. 2022, PSJ, 3, 161
Polishook, D., DeMeo, F. E., Burt, B. J., et al. 2023, PSJ, 4, 229
Pravec, P., & Harris, A. W. 2007, Icar, 190, 250
Pravec, P., Meyer, A. J., Scheirich, P., et al. 2024, Icar, 418, 116138
Raducan, S. D., & Jutzi, M. 2022, PSJ, 3, 128
Raducan, S. D., Jutzi, M., Cheng, A. F., et al. 2024, NatAs, 8, 445
Richard, D. T., Glenar, D. A., Stubbs, T. J., Davis, S. S., & Colaprete, A. 2011, P&SS, 59, 1804
Richardson, D. C., Agrusa, H. F., Barbee, B., et al. 2024, PSJ, 5, 182
Rivkin, A. S., Chabot, N. L., Stickle, A. M., et al. 2021, PSJ, 2, 173
Roth, N. X., Milam, S. N., Remijan, A. J., et al. 2023, PSJ, 4, 206
Rożek, A., Snodgrass, C., Jørgensen, U. G., et al. 2023, PSJ, 4, 236
Scheirich, P., Pravec, P., Meyer, A. J., et al. 2024, PSJ, 5, 17
Shestakova, L., Serebryanskiy, A., & Aimanova, G. 2023, Icar, 401, 115595
Stickle, A. M., Kumamoto, K. M., Graninger, D. M., et al. 2025, PSJ, 6, 38
Thomas, C. A., Naidu, S. P., Scheirich, P., et al. 2023a, Natur, 616, 448
Thomas, C. A., Rivkin, A. S., Wong, I., et al. 2023b, LPICo, 2851, 2588
Weaver, H. A., Sunshine, J. M., Ernst, C. M., et al. 2024, PSJ , 5, 43
Yoshikawa, M., Kawaguchi, J., Fujiwara, A., & Tsuchiyama, A. 2015, in Asteroids IV, ed. P. Michel, F. E. DeMeo, & W. F. Bottke (Tucson, AZ: Univ. Arizona Press), 397
Zinzi, A., & Della Corte, V. 2023, Documentation for Data from the Light Italian Cubesat for Imaging of Asteroids (LICIACube) Mission, v1.0, NASA Planetary Data System, doi:10.26007/0C5E-JK76
Zubko, E., Muinonen, K., Muñoz, O., et al. 2013, JQSRT, 131, 175
Zubko, E., Videen, G., Zubko, N., & Shkuratov, Y. 2017a, JQSRT, 190, 1
Zubko, E., Weinberger, A. J., Zubko, N., Shkuratov, Y., & Videen, G. 2017b, OptL, 42, 1962